Journal of *Marine Science and Engineering*

MDPI

Article

An Adaptive Nudging Scheme with Spatially Varying Gain for Improving the Ability of Ocean Temperature Assimilation in SPEEDY-NEMO

Yushan Wang [1,2], Fei Zheng [1,*], Changxiang Yan [1] and Muhammad Adnan Abid [3,4]

[1] State Key Laboratory of Earth System Numerical Modeling and Application, Institute of Atmospheric Physics, Chinese Academy of Sciences, Beijing 100029, China; wangyushan@mail.iap.ac.cn (Y.W.)
[2] University of Chinese Academy of Sciences, Beijing 100049, China
[3] Atmospheric, Oceanic and Planetary Physics (AOPP), Department of Physics, University of Oxford, Oxford OX1 3PU, UK
[4] National Centre for Atmospheric Science (NCAS), Oxford OX1 3PU, UK
* Correspondence: zhengfei@mail.iap.ac.cn

Abstract

Nudging remains a cost-effective data assimilation technique in coupled climate models, yet conventional schemes with fixed spatial strengths struggle to represent heterogeneous ocean processes. This study introduces an adaptive nudging framework in which a spatially varying gain matrix dynamically balances model and observational errors, providing a more physically consistent determination of nudging coefficients. Implemented in the SPEEDY-NEMO coupled model, the method is systematically evaluated against a traditional latitude-dependent scheme. Results show substantial improvements in subsurface temperature assimilation across key regions, including the Niño3.4, tropical Indian Ocean, North Pacific, North Atlantic, and northeastern Pacific. The most pronounced gains occur above and within the thermocline, where strong stratification renders fixed nudging strengths inadequate, yielding a 20–30% reduction in RMSE and a 30–50% increase in correlation. In mid- to high-latitude regions, improvements extend to greater depths, consistent with deeper thermocline structures. The adaptive framework corrects both systematic bias and variance, enhancing not only the mean state but also variability representation. Additional benefits are found in salinity, currents, and sea surface height, demonstrating that spatially adaptive nudging provides a more effective and practical alternative for improving ocean state estimation in coupled models.

Keywords: adaptive nudging; ocean state estimation; ocean temperature assimilation; coupled climate models; simulation and evaluation

Academic Editor: Jean-Louis Pinault

Received: 19 November 2025
Revised: 11 December 2025
Accepted: 16 December 2025
Published: 19 December 2025

1. Introduction

Accurate assimilation of ocean temperature fields is essential for improving the predictive skill of climate models, as anomalous variations in ocean temperature drive major climate phenomena such as the El Niño–Southern Oscillation (ENSO) and the Atlantic Meridional Overturning Circulation (AMOC). Beyond these large-scale modes, temperature anomalies exert fundamental control on key oceanic processes by regulating density stratification and mixed-layer depth [1], shaping the thermocline and vertical heat transport [2], and modulating deep-water formation that determines the strength of the AMOC [3]. These processes govern basin-scale circulation and air–sea exchanges of heat, freshwater, and

carbon, thereby linking local thermal variability to global climate responses. Consequently, temperature anomalies influence not only global heat redistribution but also regional precipitation patterns and the steric component of sea-level rise [4–6]. Taken together, these findings underscore that accurate representation of ocean thermal states—from surface SSTs to subsurface heat content—is indispensable for constraining physical processes, reproducing observed variability, and supporting reliable seasonal-to-decadal climate predictions. Building on this premise, precisely simulating ocean circulation and thermal states becomes essential not only for understanding the dynamics of the global climate system but also for improving its long-term predictability [7]. However, current numerical models still exhibit significant biases in reproducing ocean temperature fields, circulation structures, and climate indicators, primarily due to simplified physical process parameterizations and initial field errors [8]. To address these issues, data assimilation techniques, particularly the nudging method, which integrates observational data with model outputs, have become vital tools for correcting model biases and improving simulation accuracy. Owing to its relatively low computational cost and ease of implementation, nudging has been widely applied in ocean and climate models [9–13].

In the practical implementation of oceanic and atmospheric models, latitude-dependent nudging methods typically employ a fixed spatial distribution strategy (e.g., maintaining constant strength in the tropical and subtropical regions and linearly decreasing towards the poles) to determine the assimilation strength coefficient. This approach implicitly assumes that model and observational errors are uniformly distributed in space, but this assumption does not align with the complexity of actual ocean processes [14]. Ocean processes exhibit significant spatial heterogeneity, especially in the error characteristics of the tropical thermocline and deep ocean regions at mid- to high latitudes, which makes it difficult for latitude-dependent nudging methods to adapt effectively [15]. This limitation not only leads to insufficient assimilation constraints in the thermocline (e.g., the 100–200 m depth region) but may also cause "over-convergence" in certain areas due to improper assimilation strength settings [14,16]. Furthermore, it should be noted that the nudging method, as a "Newtonian relaxation" technique, fundamentally operates by adding a linear adjustment term to the model state variables to nudge them toward observations. This approach inherently corrects the model state directly rather than adjusting the underlying physical processes responsible for biases (e.g., vertical mixing, advective transport). In observation-sparse and dynamically complex ocean subsurface regions (such as the thermocline), this "process-agnostic" correction may face inherent structural challenges: if the state adjustments are inconsistent with the model's intrinsic physical constraints, it may be difficult to establish a stable new equilibrium, potentially inducing dynamical imbalances or unphysical transient responses.

To address these issues, a promising direction is to develop nudging schemes with spatially adaptive coefficients that reflect local model and observational uncertainties. The core idea of weighting by error variances, akin to the gain in optimal interpolation or Kalman filtering, has been explored in different data assimilation contexts [17]. For example, it has been used by Chen in the ensemble particle filter to deal with non-Gaussian, and by Liu to derive the spatial variable coefficient of tidal elevation assimilation in barotropic model [14].

Building on this foundational concept, the present study implements and evaluates a fully three-dimensional, spatially adaptive nudging scheme within the SPEEDY-NEMO coupled ocean-atmosphere climate model. Our method constructs a gain matrix from climatological estimates of model and observational error variances and uses it to scale the nudging strength at each grid cell throughout the integration. Unlike studies focused on algorithmic development for sequential filters or single-variable assimilation in uncoupled

models, our work aims to provide a practical, physically interpretable adaptive nudging framework for long-term coupled climate simulations. We systematically assess its impacts not only on ocean temperature but also on cross-dependent variables such as salinity, currents, and sea surface height, and examine its impacts on atmospheric fields.

By conducting the comparison experiments with a traditional latitudinally uniform nudging strength scheme (Latmean), this study evaluates the improvement of the ocean temperature field and related climate processes from multiple perspectives, including error structure decomposition, regional response differences, and the reproduction of key climate indices [14,18]. The results demonstrate that the adaptive approach effectively reduces root-mean-square errors by 20–30% and enhances model–observation correlations by 30–50% in key regions such as the Niño3.4, tropical Indian Ocean, North Pacific, and North Atlantic. More importantly, the evaluation elucidates deeper physical mechanisms: the refined ocean temperature field exerts positive cross-variable influences on salinity, currents, and sea surface height anomalies, while also exposing a structural limitation inherent to the "ocean-only" assimilation framework within a coupled model context—specifically, its capacity to perturb atmospheric precipitation responses. Consequently, this study not only confirms the potential of spatially adaptive nudging for enhancing ocean state estimation in coupled climate models, but, more critically, by delineating the scheme's integrated effects and intrinsic constraints in a coupled system, furnishes essential physical insights for the development of more consistent and physically coherent air–sea coupled data assimilation.

The remainder of this paper is organized as follows. Section 2 describes the model configuration, datasets, and methodology. Section 3 outlines the experimental design and evaluates the effectiveness of the proposed scheme in improving ocean temperature fields. Section 4 extends the assessment to other oceanic variables, including salinity, currents, and sea surface height, and also examines the partial atmospheric responses. Section 5 provides concluding remarks and directions for future work.

2. Model, Methods, and Data

2.1. Coupled Model Description

This study employs an intermediately complex coupled model, SPEEDY–NEMO, comprising an atmospheric component (SPEEDY) and an oceanic component (NEMO), coupled through the OASIS3 coupler [19]. The atmospheric module, SPEEDY (Simplified Parameterizations, privitivE-Equation Dynamics [20–22], is a spectral model with T30 truncation (approximately 3.75° × 3.75°) and 8 vertical σ-levels.

The oceanic component is based on the NEMO framework (Nucleus for European Modelling of the Ocean [23] with a nominal resolution of ~2° on the ORCA2 tripolar grid, enhanced to ~0.5° in the tropics. The vertical grid consists of 31 z-levels, with layer thickness increasing from 10 m at the surface to 500 m in the deep ocean. Sea ice is represented using the LIM (Louvain-la-Neuve Ice Model) model, which accounts for both thermodynamic and dynamic processes. While offering a useful and highly efficient framework for coupled climate studies, the model is constrained by several inherent limitations: the coarse resolution and simplified physics of SPEEDY restrict its ability to resolve detailed atmospheric circulation features, whereas the relatively low resolution of NEMO hampers the simulation of mesoscale variability and sharp oceanic fronts.

2.2. Adaptive Nudging Method

The nudging method is a cost-effective and easy-to-implement data assimilation technique. Initially applied in meteorology by Anthes [24], it was later introduced into oceanography by Holland and Malanotte-Rizzoli [25] and Verron [26]. Latitude-dependent nudging schemes typically adopt fixed spatial distributions of relaxation coefficients. For

example, within the tropical–subtropical belt (30° S–30° N), an optimal constant coefficient (α_{base}) is determined through preliminary experiments and then linearly reduced toward the poles, vanishing near 60° N/S [27]. Vertically, the assimilation strength generally follows an exponential decay profile. While computationally simple, this fixed structure implicitly assumes spatial homogeneity of model and observational errors, preventing the method from capturing spatial heterogeneity in model performance and observational quality. As a result, biases remain pronounced in subsurface regions such as the thermocline and in mid- to high-latitude oceans.

To overcome these limitations while preserving the computational efficiency and ease of implementation of traditional nudging for long-term climate integrations, we choose to enhance its standard framework. Specifically, we retain the exponential attenuation trend of the coefficient with depth and the latitudinal reference variation, but introduce an adaptive mechanism based on a spatially varying gain matrix. The scheme introduces a gain matrix K_i, which adaptively adjusts the nudging strength according to local error characteristics:

$$K_i = \frac{P_i}{P_i + R_i} \tag{1}$$

where P_i denotes the model error matrix and R_i the observational error matrix. The model error reflects uncertainties intrinsic to the model simulations, while the observational error reflects the reliability of assimilated data.

Both matrices are estimated from root-mean-square errors (*RMSE*) between free-running model outputs and observations, which can be expressed as

$$RMSE(x) = \sqrt{\frac{1}{N}\sum_{i=1}^{N}\left(x^{(i)} - x_{obs}^{(i)}\right)^2}, \tag{2}$$

where N is the total number of temporal samples. Specifically, P_i is derived from the RMSE between the free-running model outputs and the reference observations (ORAS5), while R_i is derived from the *RMSE* between the assimilated data (GODAS) and the same reference observations. This estimation based on static climate states aims to address the persistent system model bias in long-term coupled climate integration, rather than relying on anomalous events with instantaneous changes. The climatological P_i field therefore represents the spatial structure of long-term model deficiencies and guides the adaptive nudging to apply stronger corrections where biases are recurrent.

When model errors dominate ($P_i \gg R_i$), the gain coefficient K_i approaches 1, thereby strengthening the observational constraint. Conversely, when observational errors dominate, K_i decreases, weakening the adjustment. This dynamic weighting mechanism allows assimilation strength to vary spatially in a physically consistent way, thereby improving overall assimilation accuracy. The final nudging strength at each grid point is given by

$$\alpha = \alpha_{base} \times K_i \tag{3}$$

where α_{base} denotes the baseline nudging coefficient and K_i the spatially varying gain factor (Figure 1). For fair comparison, the combined field $\alpha_{base} \times K_i$ was zonally averaged to construct a nudging coefficient that retains the same vertical exponential decay as the baseline scheme but varies only with latitude, analogous to traditional latitude-dependent formulations (hereafter the Latmean-method). This design allows the comparison between the two schemes to isolate the impact of three-dimensional spatial variability introduced by K_i, relative to the traditional approach that prescribes a fixed latitudinal structure.

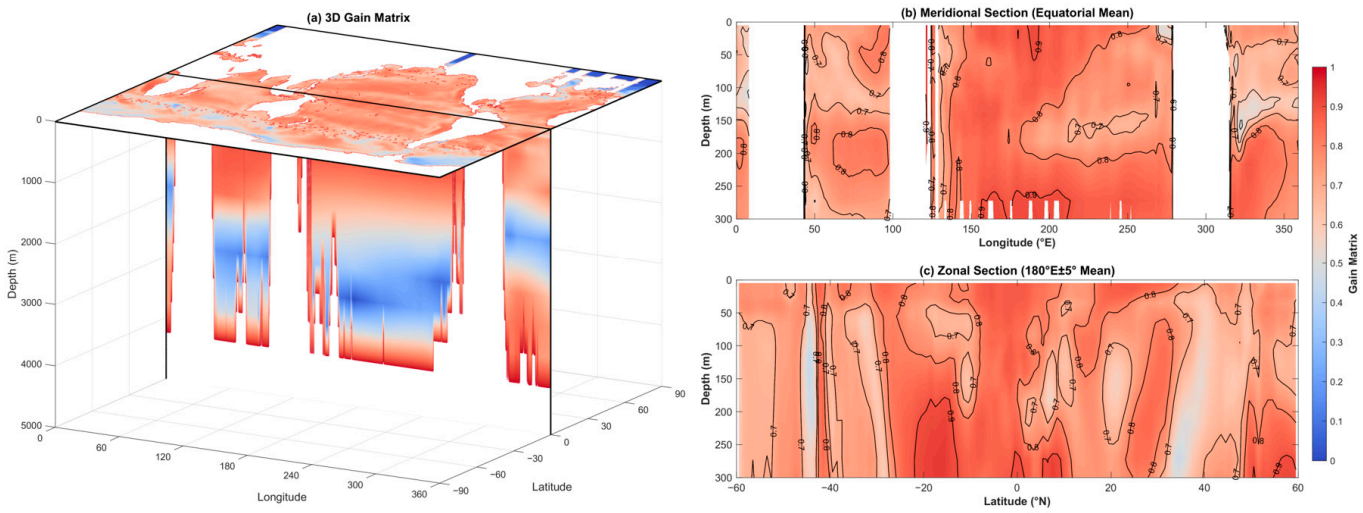

Figure 1. The gain matrix applied to the nudging strength is constructed from model errors, estimated by comparing the ORAS5 ocean temperature dataset with the model free-run outputs, and observational errors, estimated using NOAA assimilation data. Panel (**a**) illustrates the three-dimensional structure of the gain matrix, with the horizontal plane showing the surface distribution and the vertical plane showing the equatorial cross-section. Panel (**b**) presents the gain matrix cross-section along the equator within the 0–300 m depth range, while panel (**c**) shows the cross-section along 180° longitude.

To determine a baseline nudging coefficient appropriate for this study and compatible with the SPEEDY-NEMO model, a series of preliminary sensitivity experiments were conducted. By assessing the assimilation results under different nudging strengths and comprehensively comparing their root-mean-square error, correlation coefficients, and characteristics of output variability, the optimal nudging strength for the SPEEDY-NEMO model was determined to be 3 day^{-1}. Two primary experiments were designed (Table 1):

(1) the adaptive (K) method, which incorporates the full spatial structure of the gain matrix to dynamically determine nudging strength at each grid cell.
(2) the conventional (Latmean) method, wherein the nudging coefficient varies solely with latitude.

Table 1. Experimental design of nudging schemes. The adaptive (K) method employs a full 3D spatially varying gain matrix to determine the nudging coefficient, whereas the traditional (Latmean) method uses its zonal average, resulting in a coefficient that varies only with latitude.

Experiment	Nudging Coefficient Formula
Expt 1: K Method	$\alpha_k = \alpha_{base} \times K_i$
Expt 2: Latmean-Method	$\alpha_{latmean} = \lvert\alpha_{base} \times K_i\rvert_{Latmean}$

This comparative framework effectively isolates the contribution of spatially resolved error adaptation, in contrast to the zonal-mean approximation inherent to traditional approaches. Figure 2 illustrates the construction of nudging strength using sea surface temperature (SST) as an example, including the spatial distribution of the surface-layer gain matrix (Figure 2a), the nudging strength derived from the gain-matrix-based adaptive method (Figure 2b), and the nudging strength based on the traditional latitude-dependent scheme (Figure 2c).

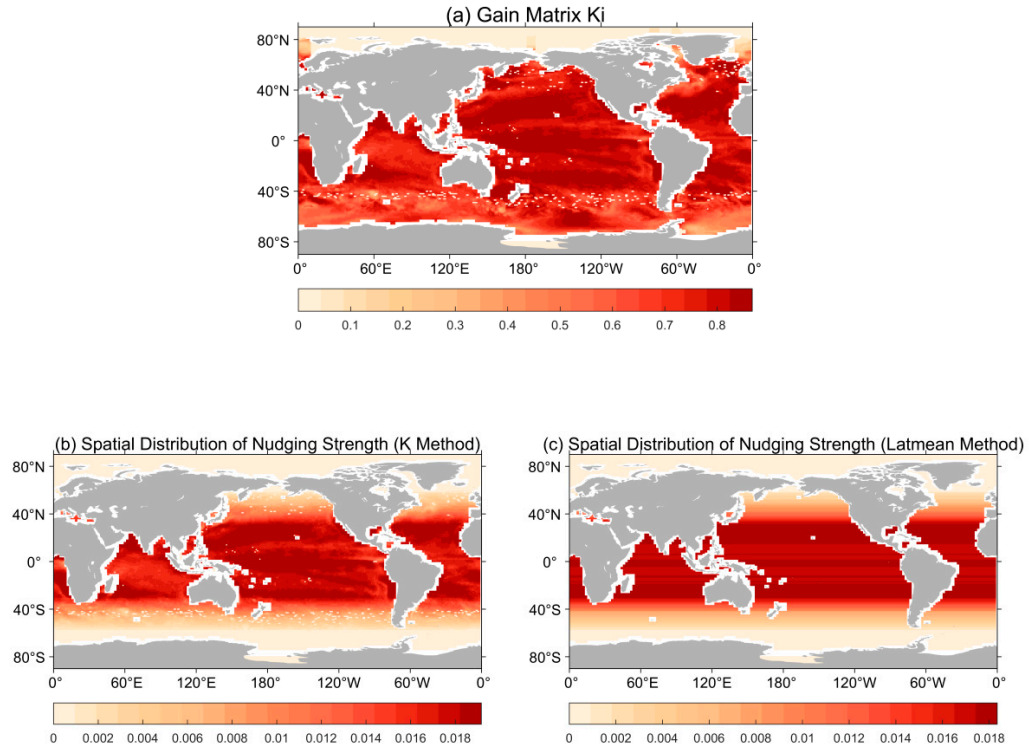

Figure 2. Construction of nudging strength illustrated with sea surface temperature (SST) as an example. (**a**) Spatial distribution of the surface-layer gain matrix. (**b**) Spatial distribution of nudging strength derived from the gain-matrix-based adaptive method (K method). (**c**) Spatial distribution of nudging strength based on the traditional latitude-dependent scheme (Latmean method).

2.3. Evaluation Methods

The core evaluation metrics include the root-mean-square error (RMSE) and the correlation coefficient (R). Both RMSE and R are evaluated by comparing the results of the nudging experiments with the reference observations. RMSE directly quantifies the difference between model outputs and observations, while R measures the temporal consistency between simulated and observed variations. Based on these two metrics, we further compute the correction rate of the K method relative to the Latmean method:

$$P_{RMSE} = \frac{RMSE_{latmean} - RMSE_k}{RMSE_{latmean}} \tag{4}$$

$$P_R = \frac{R_K - R_{latmean}}{1 - R_{latmean}} \tag{5}$$

RMSE can be decomposed into multiple components, enabling identification of the specific sources of differences between model outputs and observations [28]. The decomposition of RMSE is defined as

$$RMSE\ (\ f, x\ )^2 = \left(\bar{f} - \bar{x}\right)^2 + s_f^2 + s_x^2 - 2\ s_f\ s_x\ R \tag{6}$$

where $\bar{f}$ and $\bar{x}$ denote the mean values of the model outputs and observations, respectively, while s_f and s_x represent their standard deviations, and R is the correlation coefficient between f and x. Since the standard deviations are typically several orders of magnitude larger than the means, the RMSE^2 can be separated into a bias component ($(\bar{f} - \bar{x})^2$) and a variance component ($s_f^2 + s_x^2 - 2\ s_f\ s_x\ R$). Since R is always less than 1, so $s_f^2 + s_x^2 - 2\ s_f\ s_x\ R \geq (s_f - s_x)^2$, variations in the variance component can be inter-

preted as the squared difference between the standard deviations of the model outputs and the observations. The bias component represents the local systematic deviation between the simulated results and the observations, whereas the variance component characterizes differences in variability, thereby serving as a key indicator of the robustness of the simulation performance.

2.4. Data

In this study, SPEEDY-NEMO was spun up for 1000 years until reaching equilibrium [29]. After stabilization, a 420-month free integration was conducted to quantify model errors and provide initial conditions for assimilation experiments.

To ensure a controlled, fair, and reproducible experiment that avoids the complications arising from the sparsity, irregular sampling, and interpolation uncertainties inherent in raw observational datasets, we employed well-established ocean reanalysis products for both model evaluation and error estimation, and thereby to properly evaluate the improvements of the proposed spatially adaptive nudging scheme relative to the traditional latitude-dependent scheme.

Within this context, the monthly mean reanalysis data from ECMWF ORAS5 (1990–2024) [30] as the reference "truth" for validation. ORAS5 assimilates a comprehensive suite of in situ and satellite observations and has undergone extensive validation, providing a physically consistent and spatially complete estimate of the ocean state. Its independence from the SPEEDY-NEMO model makes it a suitable benchmark for identifying the model's climatological systematic biases. Therefore, the model error variance (P_i) in this experiment was derived from the climatological root-mean-square error (RMSE) between the long-term free-running model simulation and the ORAS5 reanalysis data.

The monthly mean three-dimensional ocean temperature data from the National Centers for Environmental Prediction (NCEP) Global Ocean Data Assimilation System (GODAS) is selected as the observational input for assimilation. To quantify the inherent uncertainty of this dataset, GODAS and ORAS5 can be considered practically independent, based on their fundamental differences in data assimilation frameworks, ocean model physics, and background error representations. Accordingly, the observational error (R) for the assimilated GODAS data is operationally defined as the climatological root-mean-square error (RMSE) between the GODAS fields and the ORAS5 reference.

To systematically evaluate the atmospheric response to ocean temperature assimilation and to assess the physical consistency of air–sea coupling processes, this study additionally employs several key atmospheric variables from the ERA5 reanalysis produced by the European Centre for Medium-Range Weather Forecasts (ECMWF). These include monthly precipitation, zonal wind at 850 hPa, vertical velocity, specific humidity, evaporation, and mean sea level pressure, covering the period 1990–2024 [31].

Data preprocessing steps included: temporal interpolation (from monthly to daily resolution), vertical interpolation onto the 31 z-levels of SPEEDY-NEMO, and spatial interpolation onto the ORCA2 grid. Observational errors were then obtained by calculating the RMSE between the GODAS and ORAS5 data.

3. Spatial and Vertical Improvements in Ocean Temperature Assimilation with the Adaptive Nudging

The climatological mean state provides a fundamental benchmark for assessing the performance of data assimilation schemes, as it reflects the model's ability to replicate the long-term average ocean thermal structure. Accurate representation of this mean state is crucial, since systematic biases can propagate into and distort the simulation of temporal variability and climate phenomena. To this end, we begin our evaluation by examining

the improvements in climatological sea surface temperature (SST) under the two nudging schemes. Figure 3 illustrates the performance of the K method and the Latmean method, compared with the free-run (FREE) simulation, in improving the climatology of sea surface temperature (SST). The first column (Figure 3a,c,e) shows SST bias distributions under the K method, the Latmean method, and the FREE state, respectively. Both assimilation methods substantially reduce temperature biases relative to the FREE run, particularly in the tropics and mid- to high-latitude regions. This demonstrates that incorporating nudging into the SPEEDY-NEMO model significantly corrects climatological biases. Specifically, Figure 3a,c reveal that the K method yields more pronounced bias reduction than the Latmean method across multiple regions, most notably in the tropics, the North Pacific, the North Atlantic, and the South Pacific. By contrast, the FREE simulation (Figure 3e) exhibits substantial and spatially extensive SST biases, underscoring both the necessity of assimilation in constraining the coupled model and the added value of the adaptive K method.

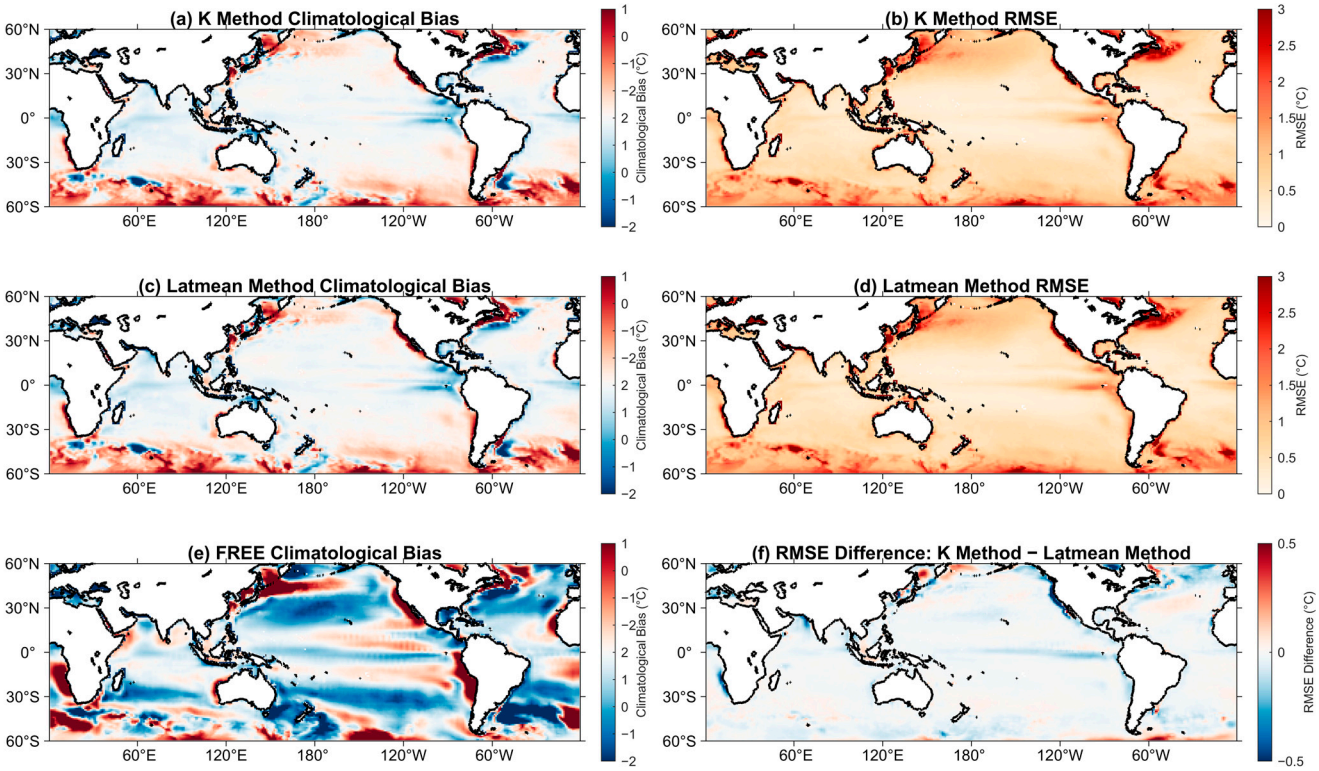

Figure 3. Climatological bias (left column) and root-mean-square error (RMSE; right column) of sea surface temperature (SST) relative to ORAS5 observations. (**a**) Climatological bias of the K method, (**c**) climatological bias of the Latmean method, and (**e**) climatological bias of the FREE run. (**b**) RMSE of the K method, (**d**) RMSE of the Latmean method, and (**f**) RMSE difference between the K method and the Latmean method. Both nudging schemes substantially reduce SST biases compared with the FREE run, with the K method yielding lower RMSE values and more pronounced improvements, particularly in the tropics and mid- to high-latitude regions.

Figure 3b,d,f present the RMSE distributions of the K method and the Latmean method relative to observations, as well as their differences. Figure 3b,d show that both methods lead to a reduction in RMSE in regions where nudging is applied. Figure 3f further highlights the RMSE difference between the two methods, demonstrating that the K method yields lower RMSE values across many regions, particularly in the tropics.

Beyond surface temperature, the vertical distribution of assimilation improvements is further quantified in Figure 4, which shows the correction rates of RMSE and correlation coefficients for ocean temperature in the two assimilation experiments. Figure 4 shows

the correction rates of RMSE and correlation coefficients for ocean temperature in the two assimilation experiments. The results indicate that the gain-matrix-based nudging method achieves substantial improvements over the traditional Latmean scheme (fixed latitudinal nudging strength) in the subsurface ocean (0–200 m), particularly in the tropics, the North Pacific, and the North Atlantic, where both RMSE and correlation coefficients improve by 15–20%. Figure 4 further highlights the advantages of the gain-matrix approach in tropical and mid-latitude regions, where it markedly reduces simulation errors, lowers RMSE, and enhances correlations, thereby improving both the accuracy and consistency of the simulated temperature fields. In contrast, the traditional Latmean method shows only limited improvement in these regions, retaining larger temperature biases and higher RMSE.

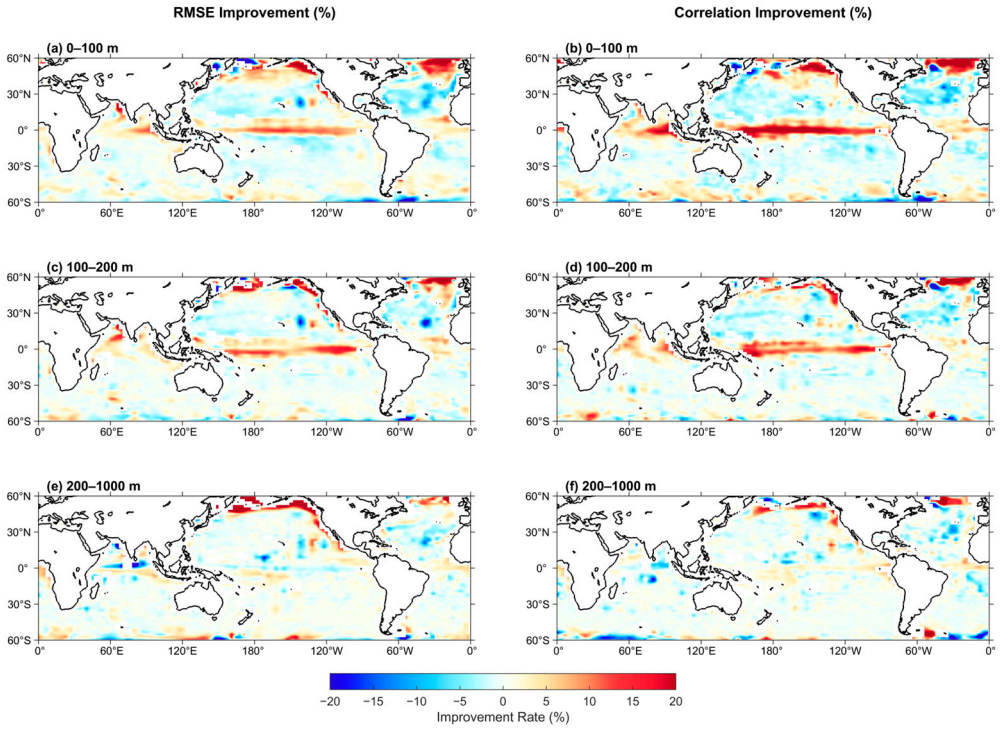

Figure 4. Global improvement rates (%) of ocean temperature between the adaptive K method and the traditional Latmean scheme, validated against ORAS5 ocean potential temperature and averaged over three depth ranges. Left column: RMSE improvement rates; right column: correlation coefficient improvement rates. Panels (**a**,**b**) correspond to 0–100 m, (**c**,**d**) to 100–200 m, and (**e**,**f**) to 200–1000 m. Warm (red) shading indicates regions where the adaptive K method outperforms the Latmean scheme (lower RMSE or higher correlation), while cool (blue) shading denotes degradation. The adaptive K method yields notable improvements in the tropics, the North Pacific, and the North Atlantic, particularly within subsurface thermocline layers.

However, Figure 4 also reveals degradation in certain regions at depths of 200–1000 m, particularly in the tropics. This likely results from the rapid decay of assimilation strength in the gain-matrix nudging method at these depths, which weakens the constraint and limits improvements in simulating the temperature field. This finding suggests that although the gain-matrix approach performs well in most regions, its effectiveness diminishes in the deep ocean, especially below the thermocline. Future work should explore strategies to enhance assimilation performance in deeper layers, with particular emphasis on strengthening constraints within and beneath the thermocline.

Surface diagnostics alone cannot determine whether improvements propagate into the subsurface ocean, where vertical stratification and the thermocline strongly regulate heat exchange. To evaluate the vertical penetration and depth dependence of the two nudging schemes, we compute vertical profiles and longitude–depth cross sections of correlation

and RMSE. Figure 5 presents vertical profiles of correlation coefficients and RMSE between simulated ocean temperatures and observations for the K method with spatially adaptive gain and the traditional Latmean method in tropical and mid–high-latitude regions. Panels i–l show the corresponding correction rates, clearly illustrating that the K method yields notable improvements near and above the thermocline compared with the Latmean scheme. In the tropics, high correlations are concentrated within the upper 100 m and decline with depth. By introducing the spatially varying gain matrix, the K method substantially enhances the simulation of temperature fields above the thermocline, achieving improvements of up to 30% in correlation coefficients. This improvement highlights the K method's ability to increase both accuracy and consistency, particularly for sea surface temperature, which more closely matches observations. However, at thermocline depths (~100–200 m), relatively large RMSE values are observed, in some cases exceeding 1 °C. This is attributed to the exponential decay of the baseline vertical nudging coefficient (as in classical nudging configurations), which leads to a rapid weakening of assimilation strength below the surface and insufficient constraint in the thermocline, leading to degraded subsurface temperature simulations [32]. Nevertheless, compared with the Latmean scheme, the K method achieves clear improvements above and within the thermocline: in the tropics, correlation coefficients increase by ~30% and RMSE decreases by ~20%, while in mid- to high-latitude regions improvements reach ~50% for correlations and ~30% for RMSE.

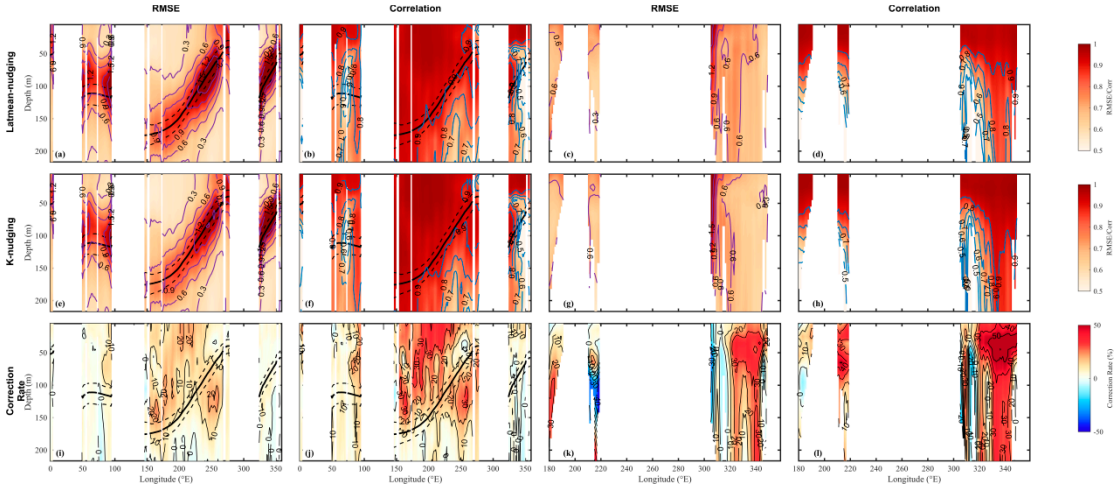

Figure 5. Longitude–depth cross sections of RMSE, correlation, and relative improvements for Latmean (**a**–**d**), K (**e**–**h**), and their differences (**i**–**l**), evaluated against ORAS5 ocean potential temperature. Panels (**a**,**b**,**e**,**f**) correspond to the equatorial belt (5° S–5° N, 0–360° E), while (**c**,**d**,**g**,**h**) show results for the North Pacific mid–high latitudes (50°–60° N, 180°–360° E). Panels (**i**–**l**) highlight the improvements of K relative to Latmean. Black dashed contours denote the 18–22 °C isotherms, with the bold line marking the 20 °C thermocline. Depth increases downward; longitude is in degrees east. Diagnostics are based on monthly data from 1990 to 2024 and the upper 20 model levels.

The third and fourth columns of Figure 5 further illustrate the correction performance of the K method relative to the Latmean method in mid- to high-latitude regions. The results show that in these regions, the K method achieves substantially greater improvements in both RMSE and correlation coefficients, particularly between 60° N and 40° N, where RMSE reductions reach ~30% and correlation improvements up to ~50%. These findings demonstrate that the K method effectively reduces temperature biases in mid- to high-latitude oceans, thereby enhancing simulation accuracy. It is noteworthy that, unlike the improvements confined mainly above the thermocline in the tropics, the performance gains in mid- to high-latitudes extend to deeper ocean layers; this is consistent with the physical

characteristics of these regions: the thermocline is inherently deeper, and oceanic processes dominated by mixed layer dynamics and convection exhibit larger regional biases. The pronounced improvement can be attributed to the spatial distribution of the gain matrix: by dynamically adjusting assimilation strength according to regional error characteristics, the K method optimizes constraints in mid- to high-latitude regions. Compared with the Latmean approach, this spatially adaptive adjustment enables more precise application of assimilation strength, ensuring a more efficient assimilation process and yielding results that more closely match observational benchmarks, thus markedly improving the fidelity of temperature field simulations.

To quantify the improvements across specific ocean areas, several key regions were selected—the Niño 3.4 region, the northeastern Pacific, the North Atlantic, and the tropical Indian Ocean—for evaluating the mean correction rates of RMSE and correlation coefficients across depth layers. Figure 6 shows that at the ocean surface, both RMSE and correlation coefficients exhibit positive improvements in all four regions. The RMSE correction rate increases from the surface, peaks around 50 m depth, and then declines near the thermocline. The shaded areas in the figure represent the interquartile ranges of correction rates within each region. RMSE corrections remain relatively consistent across depth layers, whereas correlation coefficient corrections are relatively concentrated and stable in shallow layers but become more divergent with increasing depth. This divergence arises because the baseline nudging coefficient decays rapidly with depth, weakening the method's ability to constrain variability and to capture the relationship between model outputs and observations at greater depths.

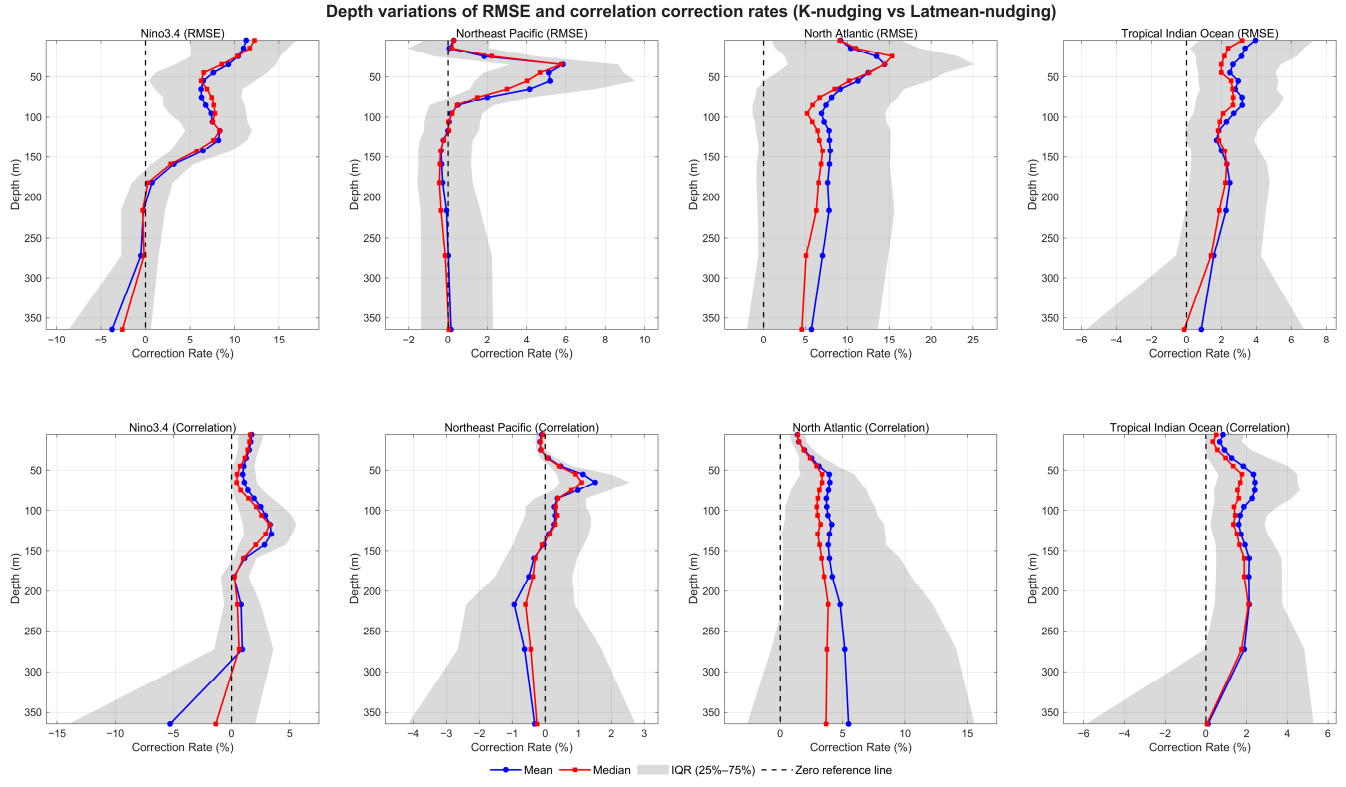

Figure 6. Depth variations in RMSE (top row) and correlation coefficient (bottom row) correction rates between the K-nudging and Latmean-nudging experiments across four representative oceanic regions: Niño3.4, Northeast Pacific, North Atlantic, and Tropical Indian Ocean. Blue lines denote the mean correction rate, red lines indicate the median, shaded gray areas show the interquartile range (25–75%), and black dashed lines represent the zero reference. Positive values indicate improved agreement with observations in the K-nudging experiment relative to the Latmean-nudging experiment.

To further investigate the sources of improvements of the K method relative to the Latmean method in ocean temperature assimilation, Figure 7 presents the root-mean-square error (RMSE) of simulated ocean temperatures and its decomposition. RMSE was calculated globally at each grid point and separated into bias and variance components to obtain their spatial distributions. The bias component reflects long-term systematic deviations of the simulations from observations, revealing the model's inherent climatological biases, while the variance component represents the model's ability to capture spatiotemporal variability. Compared with the Latmean scheme, the K method yields 20–50% improvements in both components within the regions previously identified as showing substantial benefits. However, in the 200–400 m depth range—particularly in the tropics—improvements weaken and even become negative in some areas. This indicates that in deeper layers, especially below the thermocline, the spatial adaptivity of the gain matrix is insufficient to maintain consistent corrections, highlighting a limitation of nudging methods where assimilation strength decays too rapidly with depth.

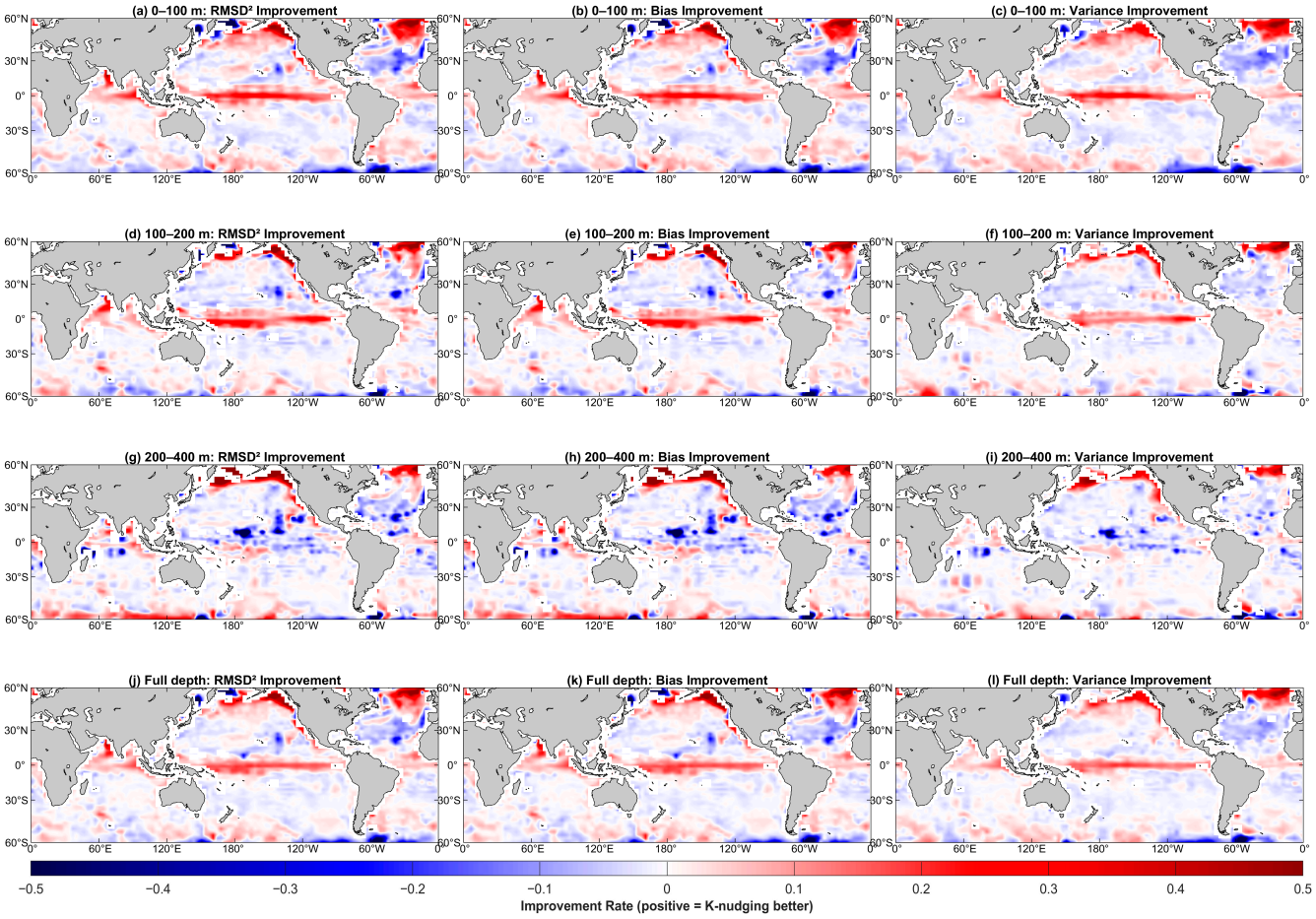

Figure 7. Depth-averaged spatial distributions of three improvement rates comparing the K-nudging and Latmean-nudging schemes. Rows correspond to depth ranges: (**a**–**c**) 0–100 m, (**d**–**f**) 100–200 m, (**g**–**i**) 200–400 m, and (**j**–**l**) full depth (0–400 m). Columns show, from left to right: $RMSE^2$ improvement rate, bias-term improvement rate, and variance-term improvement rate.

Following the investigation into the spatial patterns of RMSE and its components, we now examine their temporal evolution to assess whether the improvements offered by the adaptive scheme are consistent over time. Figure 8 analyzes the temporal evolution of RMSE between the two nudging schemes and observations. Panel a shows annual mean RMSE time series, indicating that the K method consistently achieves lower RMSE than the latitude-dependent nudging scheme across all selected regions. To identify the

sources of this improvement, panel b presents bar plots of RMSE^2 decomposed into bias and variance components, along with line plots of their ratios. In most regions and years, variance exceeds bias, confirming that variance dominates the contribution to RMSE. Panel c illustrates the annual mean absolute bias, showing that the K method reduces bias relative to the Latmean method in all regions. The fluctuations are likely associated with "unexpected" ocean temperature variability during climate events, such as ENSO, when strong nonlinear ocean–atmosphere interactions occur [33,34]. Because nudging is inherently a linear correction method, it may struggle to fully capture such nonlinear processes, leading to reduced assimilation performance during these episodes. Panel d shows the time series of absolute standard deviation as an indicator of simulated SST variability. The K method generally outperforms the latitude-dependent scheme, although variance remains the dominant contributor to RMSE, highlighting the need for further improvement in variance representation.

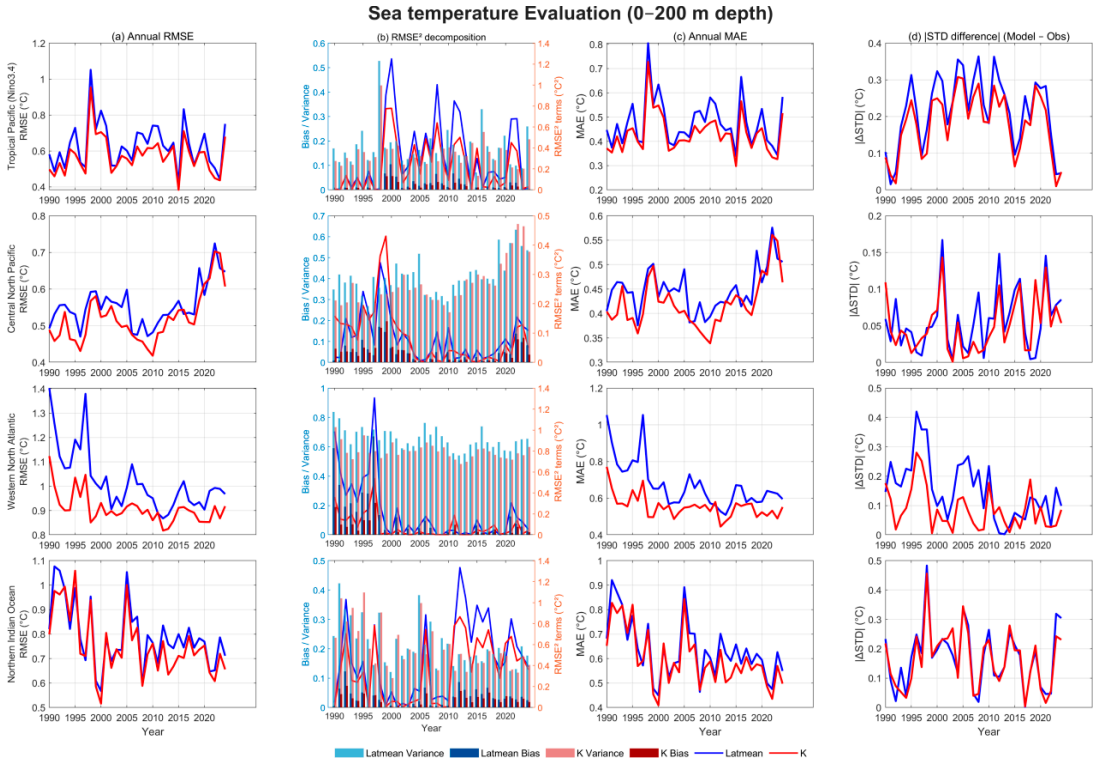

Figure 8. Comparative assessment of the Latmean-nudging scheme (blue) and the K-nudging scheme (red) against ORAS5 observations for upper-ocean temperature (0–200 m) during 1990–2024. Model-observation discrepancies are quantified using four metrics: (**a**) annual root-mean-square error (RMSE, °C), (**b**) decomposition of RMSE^2 into variance and bias contributions (bars, °C^2) with bias-to-variance ratios (lines), (**c**) annual mean absolute error (MAE, °C), and (**d**) absolute difference in interannual standard deviation (ΔSTD, °C). Analyses are presented for four representative regions—(i) Tropical Pacific (Nino3.4), (ii) Central North Pacific, (iii) Western North Atlantic, and (iv) Northern Indian Ocean—each corresponding to one row in the panel layout.

4. Cross-Variable Impacts of Adaptive Ocean Temperature Assimilation on Oceanic and Atmospheric Fields

As a fundamental state variable of the ocean system, temperature plays a crucial role in dynamical and thermodynamical processes, and thus improvements in its simulation inevitably propagate to other oceanic variables in coupled models [35,36]. For instance, temperature variations regulate seawater density, thereby driving ocean circulation such as the thermohaline circulation. Through their influence on evaporation and precipitation,

they also indirectly modify salinity distributions, while circulation and salinity in turn feedback on heat transport and redistribution [37–40]. Accordingly, the optimization of the ocean temperature field achieved by the spatially adaptive gain-matrix nudging method establishes a robust physical basis for improving the simulation of other key ocean variables.

In this section, key oceanic variables including salinity, currents, and sea level height were selected to compare the performance of the K method and the Latmean method, using correction rates of RMSE and correlation coefficients as evaluation metrics.

4.1. Improvements in Other Oceanic Variables

Results in Figure 9 show that the adaptive method delivers consistent improvements across most variables. For example, sea surface height anomalies (SSHA)—which are influenced by a suite of oceanic and thermodynamic variables such as currents, pressure, temperature, and salinity [41,42]—serve as a reliable diagnostic for evaluating assimilation performance. By comparing the SSHA simulated by the two methods after assimilating sea temperature with ORAS5 data, we can assess the degree of spatiotemporal consistency and verify the dynamic consistency of phenomena such as global thermocline tilt. Furthermore, during climate events like ENSO [43,44], anomalous changes in SSHA reveal important dynamic process characteristics in the tropical Pacific region, contributing to our understanding of how air–sea coupling behaviors influence the entire climate system. When the K method is applied to ocean temperature data, as shown in Figure 10, the resulting SSHA simulations exhibit smaller deviations compared to the traditional nudging method over most of the tropical Pacific. Across all examined longitudes, there is widespread improvement in both root-mean-square error (RMSE) and correlation coefficient enhancement rates.

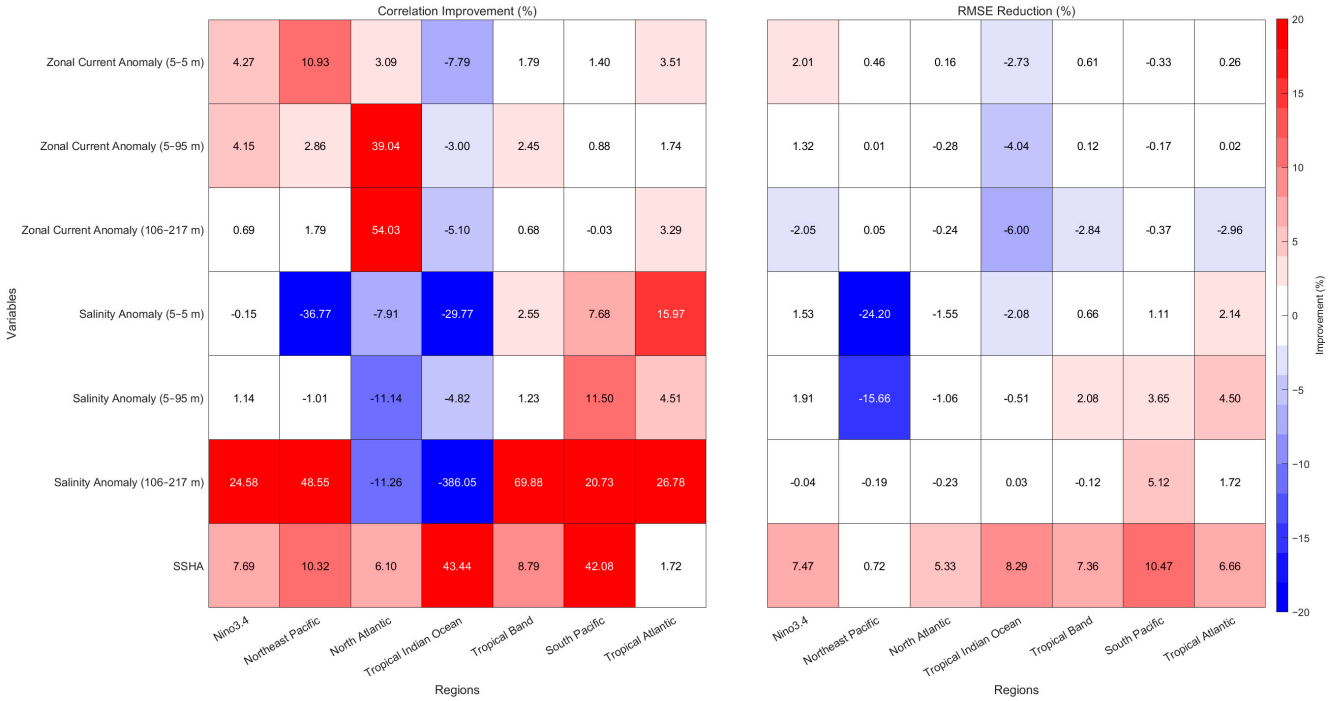

Figure 9. Regional evaluation of the relative performance of the K model against the Latmean model for multiple ocean state variables, expressed as correlation improvement (%) and RMSE reduction (%). The assessment encompasses zonal current anomalies at three depth ranges (0–5 m, 5–95 m, and 106–217 m), salinity anomalies at the same depth ranges, and sea surface height anomaly (SSHA). The metrics are computed over seven representative regions, including Nino3.4, Northeast Pacific, North Atlantic, Tropical Indian Ocean, Tropical Band, South Pacific, and Tropical Atlantic. Positive values indicate that the K model exhibits improved consistency with observations compared to the Latmean model, while negative values denote degraded skill.

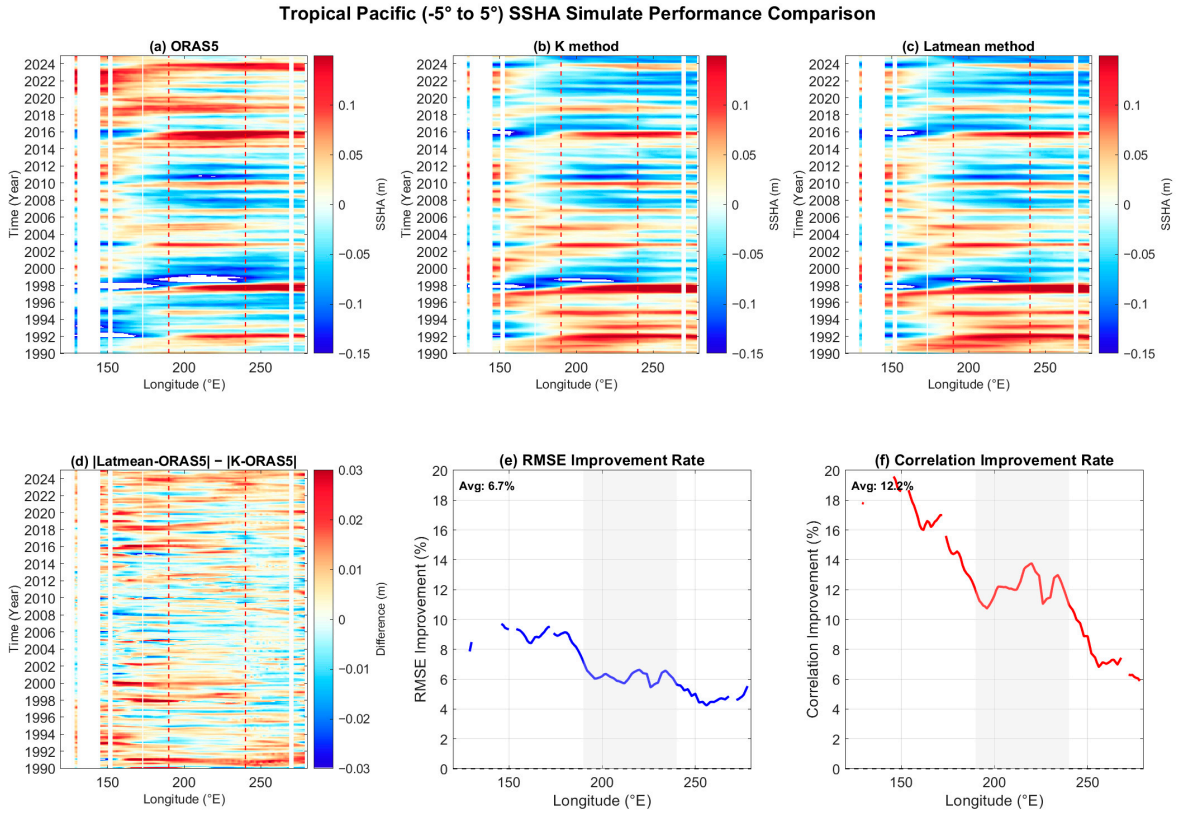

Figure 10. Comparison of simulated Sea Surface Height Anomaly (SSHA) in the tropical Pacific region (5° S–5° N). The panels show: (**a**–**c**) Longitude-time Hovmöller diagrams of SSHA for (**a**) ORAS5 reanalysis data, (**b**) simulation results from the K method, and (**c**) simulation results from the Latmean method during 1990–2024. (**d**) Absolute error difference, defined as |Latmean–ORAS5|−|K–ORAS5|. Positive values (warmer colors) indicate regions where the simulation error of the K method is smaller than that of the Latmean method. (**e**) Spatial distribution of the percentage improvement in Root Mean Square Error (RMSE) for the K method relative to the Latmean method. (**f**) Spatial distribution of the percentage improvement in correlation coefficient for the K method relative to the Latmean method. The spatial average of the improvement rates across the entire longitude range shown is annotated in the figure. The analysis indicates that the K method generally outperforms the Latmean method in simulating SSHA, particularly in reducing simulation errors and enhancing correlation with observations in the tropical Pacific region.

However, the simulated responses of salinity and zonal currents exhibit pronounced vertical differentiation (Figure 9). In the selected regions, degradations are observed in the surface layer (5–95 m), while significant positive improvements occur in the deeper layer (106–217 m), particularly for salinity in the South Pacific and zonal currents in the North Atlantic. This contrast is fundamentally linked to flux exchange mechanisms within the coupled ocean–atmosphere system and to dominant internal oceanic dynamical processes. The negative surface improvements stem from systematic biases in atmospheric forcing. At the air–sea interface, key fluxes transferred from the atmosphere to the ocean via the OASIS3 coupler directly regulate surface-layer variables: surface salinity is primarily controlled by freshwater fluxes (net precipitation minus evaporation, snowfall, and evaporation over snow/ice), while zonal currents are driven by wind stress (momentum flux). However, the atmospheric module has notable limitations: (i) its horizontal resolution (3.75° × 3.75°) is relatively coarse, leading to simulation errors; and (ii) no assimilation is applied to key atmospheric variables such as winds and precipitation, distorting the spatial distribution and intensity of freshwater fluxes and wind stress. Although ocean-temperature assimilation improves the thermal structure of the ocean, these upstream atmospheric biases remain

the dominant source of surface-level errors—for example, wind stress biases misrepresent Ekman transport [45,46], while imbalances in freshwater fluxes produce systematic departures of surface salinity from observations.

By contrast, temperature assimilation corrects subsurface thermal fields and thereby indirectly regulates vertical density gradients. This enhances both the strength and pathways of thermohaline circulation, bringing salinity distributions into closer agreement with observations, and improves geostrophic current calculations, resulting in more accurate simulations of zonal currents. At depths of 106–217 m, salinity corrections exceed 20% across most regions, highlighting the superiority of the K method relative to the Latmean scheme in temperature assimilation.

It is noteworthy that although feedback variables from the ocean to the atmosphere—such as sea surface temperature (SST) and sea-ice temperature—are improved through temperature assimilation, the simplified parameterizations and coarse resolution of the atmospheric module limit its ability to accurately respond to these signals. As a result, the closed-loop regulation of air–sea fluxes remains insufficiently accurate, emphasizing the strong dependence of surface-layer variables on atmospheric forcing. This finding delineates the boundaries of ocean-temperature assimilation and points toward future directions—namely, the development of joint ocean–atmosphere assimilation frameworks that can simultaneously correct systematic biases in atmospheric forcing fields.

4.2. Improvements in the Simulation of Oceanic Dynamical Processes

These improvements in SSHA reflect not only better-constrained oceanic mass and heat distributions but also a more realistic representation of coupled ocean–atmosphere dynamics, particularly in the tropical Pacific where ENSO dominates interannual variability [47,48]. To further quantify how the adaptive nudging influences ENSO characteristics and associated air–sea coupling, we examine the amplitude, time scale, and feedback strength of ENSO using the Niño3.4 index and equatorial zonal wind.

The basic amplitude and time-scale characteristics of ENSO are first evaluated using the Niño3.4 index (Figure 11a). The standard deviation of Niño3.4 index is 0.911 in ORAS5, while the K experiment reproduces a comparable variability amplitude of 0.880. The LATMEAN experiment also exhibits a similar amplitude (0.869), whereas the FREE simulation shows substantially weaker variability (0.694). Spectral analysis further indicates that the canonical 2–7 year ENSO band accounts for 43.11% of the total variance in ORAS5 and 43.74% in the K experiment, in close agreement with each other, while the FREE simulation contains only 32.51% of its variance within this band (Figure 11b). The LATMEAN experiment also captures a comparable fraction (43.72%). Consistently, the dominant ENSO period is about 3.05 years in ORAS5, K, and LATMEAN, but shifts to an unrealistically long 5.33 years in FREE. These results demonstrate that SST nudging effectively restores both the amplitude and the characteristic time scale of ENSO variability. While LATMEAN exhibits similar statistical variance to K, the FREE simulation exhibits a pronounced bias toward weakened and excessively low-frequency ENSO variability.

We selected strong El Niño events for analysis, the strength and phase relationship of air–sea coupling are assessed using the lagged correlation between Niño3.4 index and equatorial zonal wind at 850 hPa (u850) (Figure 11c). In ORAS5, the maximum correlation reaches 0.799 when Niño3.4 index leads u850 by one month, indicating a realistic SST-to-wind response consistent with the canonical Bjerknes feedback. The K experiment exhibits a comparable peak correlation of 0.835 at the same lag, suggesting that the nudging scheme preserves the fundamental structure of tropical air–sea interaction. The LATMEAN experiment shows a similar peak correlation (0.842), while the FREE run displays a slightly higher value (0.882). However, the apparently strong coupling in FREE occurs together

with severely underestimated ENSO amplitude and distorted spectral characteristics, implying that the large correlation does not reflect a physically realistic coupled response. Overall, the K experiment maintains a physically consistent air–sea feedback structure while simultaneously improving ENSO amplitude and time-scale characteristics.

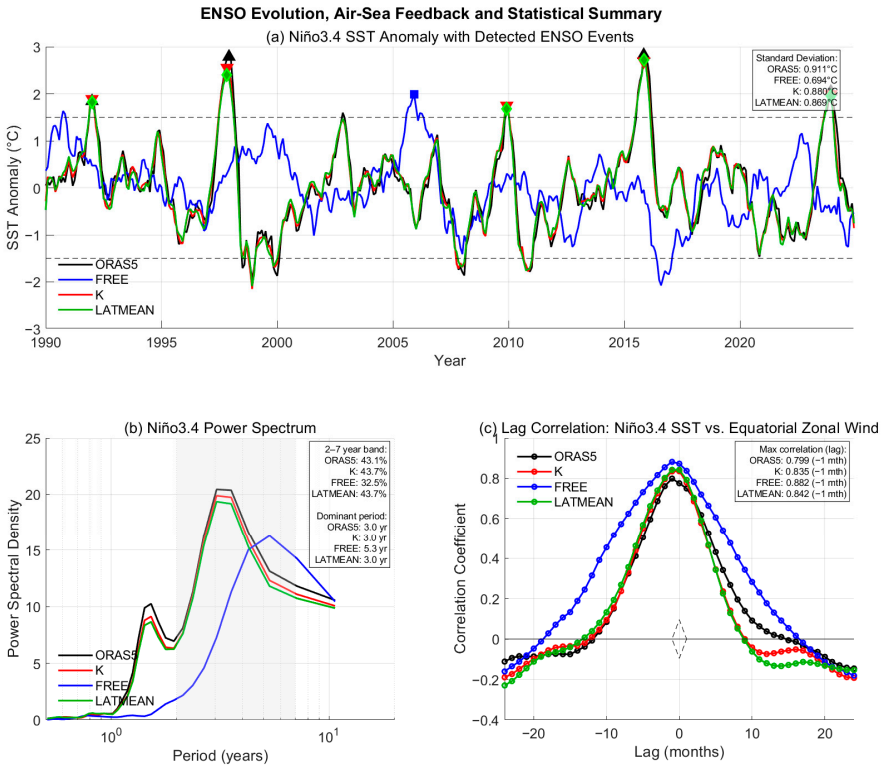

Figure 11. ENSO evolution, air–sea feedback, and statistical characteristics across four datasets. (**a**) Niño3.4 SST anomaly time series (1990–2024) from ORAS5 (black), FREE simulation (blue), K method (red), and LATMEAN method (green). Markers indicate ENSO event peaks detected in each dataset (triangles for ORAS5, squares for FREE, inverted triangles for K, diamonds for LATMEAN) using a threshold of ±1.5 °C. The text box shows standard deviations for each dataset. (**b**) Power spectral density of the Niño3.4 index, with the gray shading highlighting the 2–7 year ENSO band. The text box shows the percentage of variance in the 2–7 year band and the dominant period for each dataset. (**c**) The lag correlation between Niño3.4 SST anomalies and equatorial meridional wind (850 hPa) anomalies during the peak period of the selected strong El Ni ñ o event. The text box displays the maximum correlation coefficient and corresponding lag for each dataset.

The representation of ENSO amplitude, period, and air–sea coupling suggests that the adaptive nudging scheme adequately captures the statistical characteristics of the mode. A more stringent test, however, lies in its ability to replicate the underlying physical processes that govern ENSO evolution, namely the large-scale adjustment of the tropical Pacific ocean. We therefore investigate two key dynamical facets: the zonal propagation of sea-level signals along the equator, which reflects the integrated oceanic response, and the concomitant adjustment of the subsurface thermocline structure [49].

The zonal propagation of equatorial signals is examined using composite Hovmöller diagrams of equatorial SSH anomalies during strong ENSO events (Figure 12a–d). In ORAS5, a coherent eastward propagation from the Western Pacific (150° E) to the eastern Pacific (190° E) is clearly identified, with an equivalent low-frequency propagation speed calculated based on phase delay of approximately 0.212 m s^{-1}. The K experiment reproduces a very similar propagation speed of 0.188 m s^{-1}. The LATMEAN experiment yields an almost identical equivalent propagation speed (0.188 m s^{-1}). This indicates that the nudging scheme successfully preserves the temporal phase and signal coherence of

the large-scale equatorial adjustment process, and that both experiments capture the main characteristics of eastward adjustment. In contrast, the FREE simulation exhibits a notably slower apparent propagation speed (0.141 m s^{-1}), implying weaker intrinsic signal coherence in the model itself and a distinction in the equatorial adjustment process compared to the ORAS5 dataset. This suggests that the nudging method, by assimilating ocean temperature, not only adjusts the temperature towards the target values but also improves the simulation of oceanic physical processes.

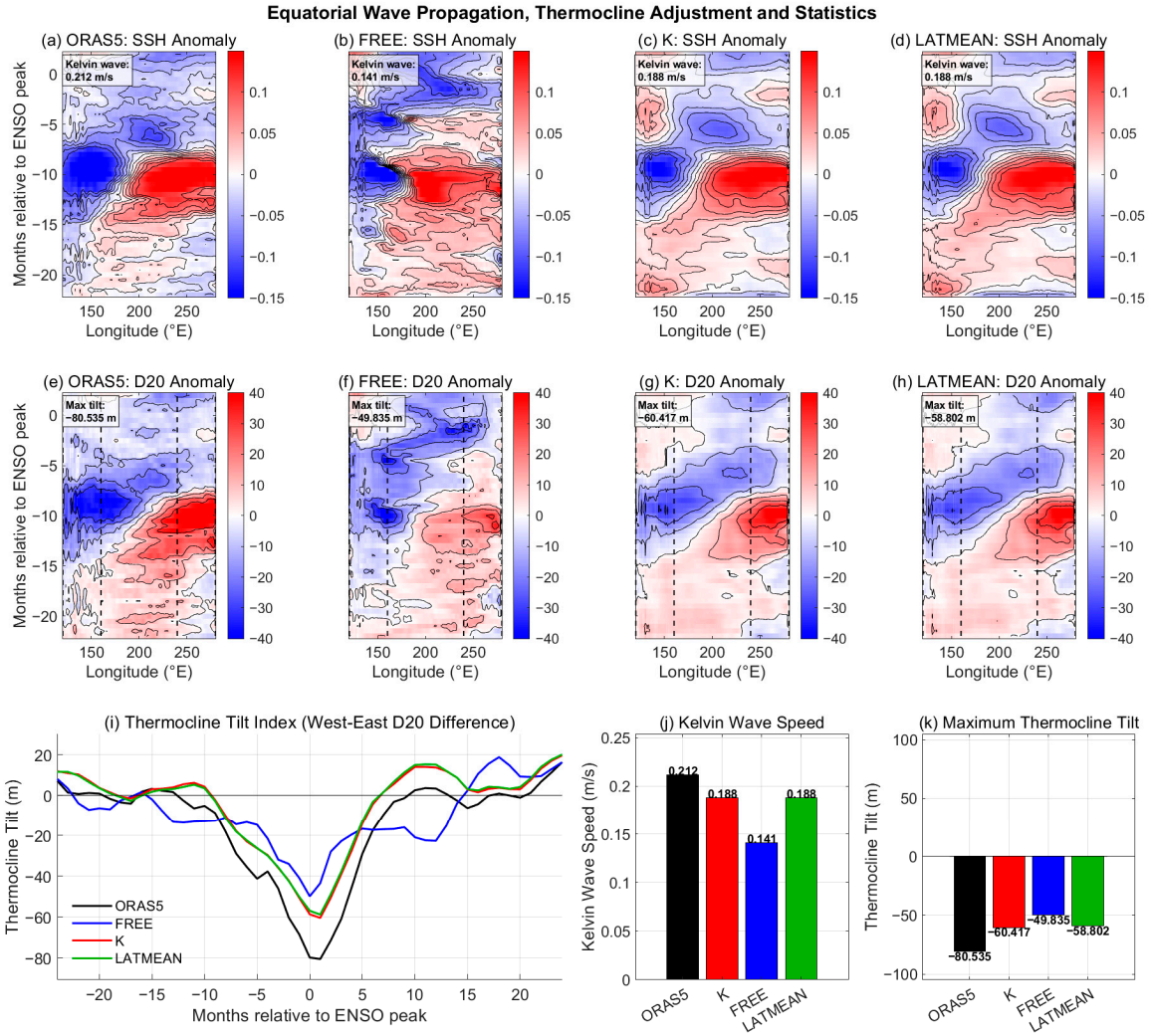

Figure 12. Equatorial wave propagation and thermocline response during ENSO. (**a**–**d**) Hovmöller diagrams of SSH anomalies along the equator (5° S–5° N) for (**a**) ORAS5, (**b**) FREE, (**c**) K, and (**d**) LATMEAN datasets, composited around ENSO event peaks (±24 months). Kelvin wave speeds (m/s) are indicated. (**e**–**h**) Corresponding Hovmöller diagrams of thermocline depth anomalies. Dashed lines mark western (120°–160° E) and eastern (240°–280° E) Pacific regions. Maximum thermocline depth gradients (m) are shown. (**i**) Evolution of thermocline depth gradient (west minus east) during ENSO composites. (**j**) Comparison of Kelvin wave propagation speeds across datasets. (**k**) Comparison of maximum thermocline depth gradients. Bars show mean values with numerical labels. All composites use ENSO events detected within each dataset (nino3.4 index threshold: ±1.5 °C).

To thoroughly evaluate the authenticity of the subsurface dynamical structure, we further analyzed the zonal slope variation in the thermocline in the tropical Pacific. The specific method involves calculating the averaged thermocline depth anomaly (typically represented by the depth of the 20 °C isotherm) for two regions: the Western Pacific (120° E–160° E) and the eastern Pacific (120° W–80° W). The anomaly value of the Western

Pacific is then subtracted from that of the eastern Pacific to obtain a time series reflecting the east–west slope of the thermocline (Figure 12e–i,k). The magnitude and sign of this difference directly characterize the zonal redistribution of subsurface heat: a larger negative value indicates that the thermocline in the Western Pacific becomes shallower relative to that in the eastern Pacific. This aligns with the classic "recharge-discharge" physical scenario during the mature phase of an El Niño event, where warm water is transported eastward from the subsurface of the Western Pacific, elevating the thermocline in the eastern Pacific [50].

During the peak phase of ENSO, the ORAS5 reanalysis data reveal a pronounced thermocline structure that is shallow in the west and deep in the east, with the peak east–west slope difference reaching −80.5 m. The experiment using the adaptive relaxation nudging scheme (K method) successfully reproduces this key dynamical feature, simulating a peak slope difference of −60.4 m. The experiment employing the traditional latitude-dependent scheme (LATMEAN) also yields a comparable magnitude (−58.8 m). In stark contrast, the free-running simulation without nudging (FREE) produces a much weaker response, with a peak slope difference of only −49.8 m. This indicates that, in the absence of observational constraints, the model alone struggles to generate a zonal subsurface mass and heat adjustment of sufficient intensity consistent with observations.

The consistency in key features between the ORAS5 data and the results of the nudging experiment (K method) confirms that the temperature nudging in the K method not only improves the surface state but also effectively propagates its influence downward, helping the model restore the subsurface dynamical adjustment processes essential for ENSO evolution. Furthermore, the K method demonstrates a certain trend of improvement over the LATMEAN method in capturing the details of this physical process.

In summary, these diagnostic results demonstrate that the proposed nudging scheme not only improves traditional statistical metrics but also enhances fundamental dynamical components of ENSO, including equatorial adjustment, subsurface thermocline recharge–discharge behavior, and the associated large-scale coupled response, while also providing some correction to biases in the model's own dynamical processes.

4.3. Atmospheric Responses and Limitations

In coupled ocean–atmosphere models, interactions occur through the exchange of momentum, heat, and freshwater fluxes. In theory, optimizing the ocean temperature field can influence atmospheric circulation and related variables via these coupled interactions [23,51,52]. This theoretical linkage is supported by our analysis of the low-level atmospheric response. As illustrated in Figure 13, which compares the time series of 850-hPa zonal wind anomalies over the Western Pacific simulated under different schemes, the anomaly evolution generated by the adaptive K method agrees more closely with reanalysis than that of the traditional Latmean method. The Western Pacific is a key region for westerly wind bursts, which are critical precursors to the development of strong El Niño events [53]. The improved wind simulation thus indicates that the refined ocean state from the K method yields a more realistic representation of directly coupled atmospheric circulation patterns. However, results in Figure 14 shows that despite improvements in the simulated wind fields due to ocean temperature, the precipitation climatology deteriorates in several key regions compared with the free-run simulation. In the Western Pacific warm pool and the equatorial eastern Pacific transition zone, the nudging method intensifies precipitation peaks, producing overly concentrated zonal bands. This reduces the spatial coherence between simulations and observations and leads to larger climatological biases than in the free run.

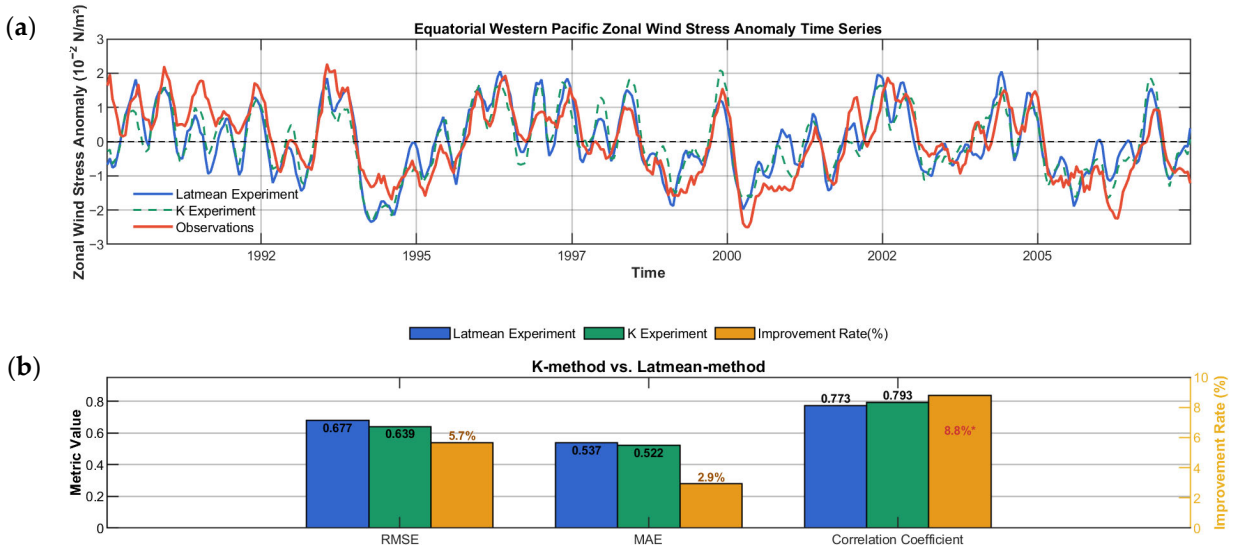

Figure 13. Evaluation of atmospheric dynamic response to ocean temperature assimilation in the equatorial Western Pacific. (**a**) Time series of regionally (120°–180° E, 5° S–5° N) averaged 850-hPa zonal wind stress anomalies. Results from the adaptive K scheme (green dashed line) and the traditional Latmean scheme (blue solid line) are compared against the ORAS5 reanalysis (red solid line). (**b**) Statistical performance comparison of the two assimilation schemes relative to ORAS5: root mean square error (RMSE), mean absolute error (MAE), and correlation coefficient (R). The orange bars indicate the improvement rate of the K-method relative to the Latmean-method. * The anomaly evolution generated by the adaptive K method agrees more closely with reanalysis than that of the traditional Latmean method.

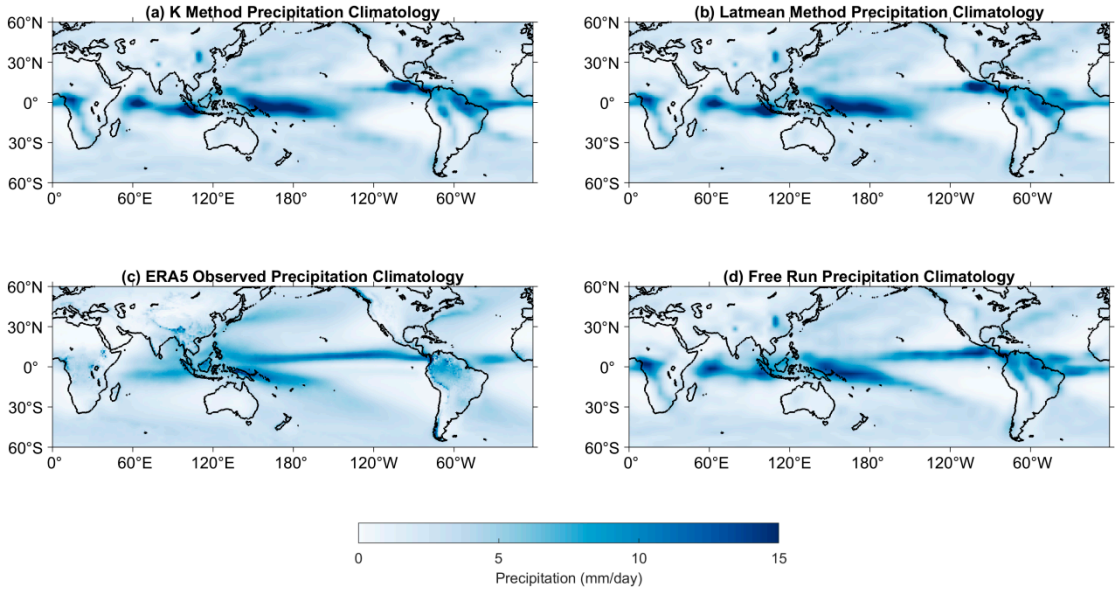

Figure 14. Climatological distribution of precipitation (1990–2024, mm/day). (**a**) K method simulation, (**b**) Latmean method simulation, (**c**) ERA5 reanalysis observations, and (**d**) free run experiment.

Several factors may explain this phenomenon. First, the SPEEDY atmospheric module has coarse horizontal resolution and simplified convective parameterizations, which limit its ability to accurately respond to the sea-surface temperature structures introduced through assimilation, thereby amplifying or misplacing air–sea interactions. Second, the simple nudging approach constrains only ocean temperature within the coupled model, without simultaneously adjusting atmospheric states such as low-level winds and precipitation. As a result, ocean temperature signals are not properly absorbed or transmitted

by the atmosphere, leading to degraded precipitation simulations. This limitation is consistent with the evaluation of SPEEDY-NEMO by Ruggieri [29], who found that although the model captures large-scale precipitation climatology, it exhibits substantial regional biases—such as underestimated South Asian monsoon rainfall, fragmented East Asian monsoon structures, and positive biases in Southern Hemisphere monsoons. To elucidate the physical mechanisms responsible for the degradation in precipitation simulation and to assess the inherent limitations of the "ocean-only" assimilation strategy within a coupled framework, we conducted a series of diagnostic analyses, focusing on air–sea flux feedbacks and large-scale atmospheric circulation responses.

We first examined whether the fundamental process of oceanic moisture supply to the atmosphere remains physically consistent under the adaptive nudging assimilation. Figure 15 compares the differences in sea surface temperature (ΔSST), latent heat flux (ΔLHF), and precipitation (ΔPrecip) between the K-scheme and the free-running experiment. SST is a key factor regulating surface latent heat flux (SLHF): over most oceanic regions, an increase in SST enhances sea surface evaporation, while LHF essentially represents the latent heat flux transferred from the ocean to the atmosphere via evaporation. Therefore, changes in SST directly drive variations in LHF [54]. Figure 15 shows that the spatial patterns of ΔSST and ΔLHF exhibit a high degree of co-variability, with consistent signs over approximately 72.1% of the oceanic grid points between 60° S and 60° N (Figure 15d). This significant sign consistency indicates that the SST changes induced by adaptive nudging lead to physically coherent responses in surface evaporation. Consequently, the degradation in precipitation cannot be attributed to the disruption of atmospheric moisture source feedback SST-driven evaporation.

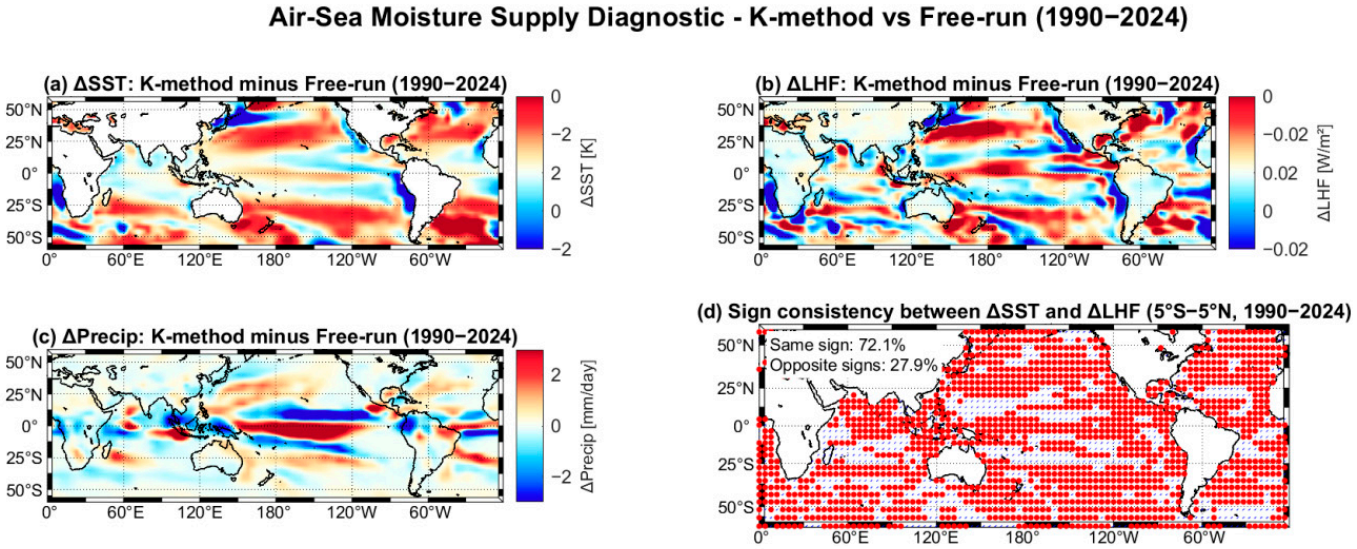

Figure 15. Air–sea moisture supply diagnostic comparing the K-method and free-run simulations. (**a**) Difference in sea surface temperature (ΔSST = K-method minus free-run) over the latitude range of 60° S–60° N. (**b**) Difference in latent heat flux (ΔLHF) between the two methods. (**c**) Difference in precipitation rate (ΔPrecip). (**d**) Sign consistency analysis between ΔSST and ΔLHF differences, where red dots indicate grid points with the same sign (both positive or both negative) and blue slashes indicate opposite signs. The statistical summary (upper left) shows the percentage of grid points with consistent versus opposing signs.

Changes in latent heat flux directly affect atmospheric moisture content and convective activity, thereby modulating precipitation patterns [55]. According to the research conclusions of Tong et al., [52] the pathway through which sea surface temperature drives precipitation follows a classical propagation mechanism: bias propagation starts from SST

anomalies (ΔSST) to near-surface specific humidity anomalies (Δq), then to surface latent heat flux anomalies (ΔLHF), and further influences the lower-tropospheric dynamical fields (vertical velocity and zonal wind) within the atmospheric module, ultimately propagating to precipitation anomalies. A comparison between Figure 15b,c reveals distinct spatial patterns between ΔLHF and ΔPrecip. This indicates that, given the fundamentally sound physical process of oceanic moisture supply to the atmosphere, precipitation biases must originate from subsequent atmospheric dynamical adjustments, particularly through the redistribution of moisture and the modulation of large-scale vertical motion.

To diagnose this response, we further analyzed the structure of the tropical Walker Circulation. Figure 16 presents longitude–height cross-sections of zonal wind averaged over the equatorial band (5° S–5° N). Both the free-running and K-scheme experiments successfully reproduce the basic structure, but their intensities are systematically weaker than those in the ERA5 reanalysis (Figure 16a–c), reflecting inherent limitations of the intermediate-complexity SPEEDY atmospheric model in representing tropical dynamics. Compared to this baseline state, the introduction of SST nudging leads to a notable strengthening of zonal wind in the upper levels around 100° E–160° W and in the lower levels around 160° W–60° W. This indicates that SST changes successfully drive adjustments in the wind fields associated with the Walker Circulation. Combined with the analysis of Figure 11 presented earlier, nudging assimilation of SST directly improves the simulation of zonal wind fields.

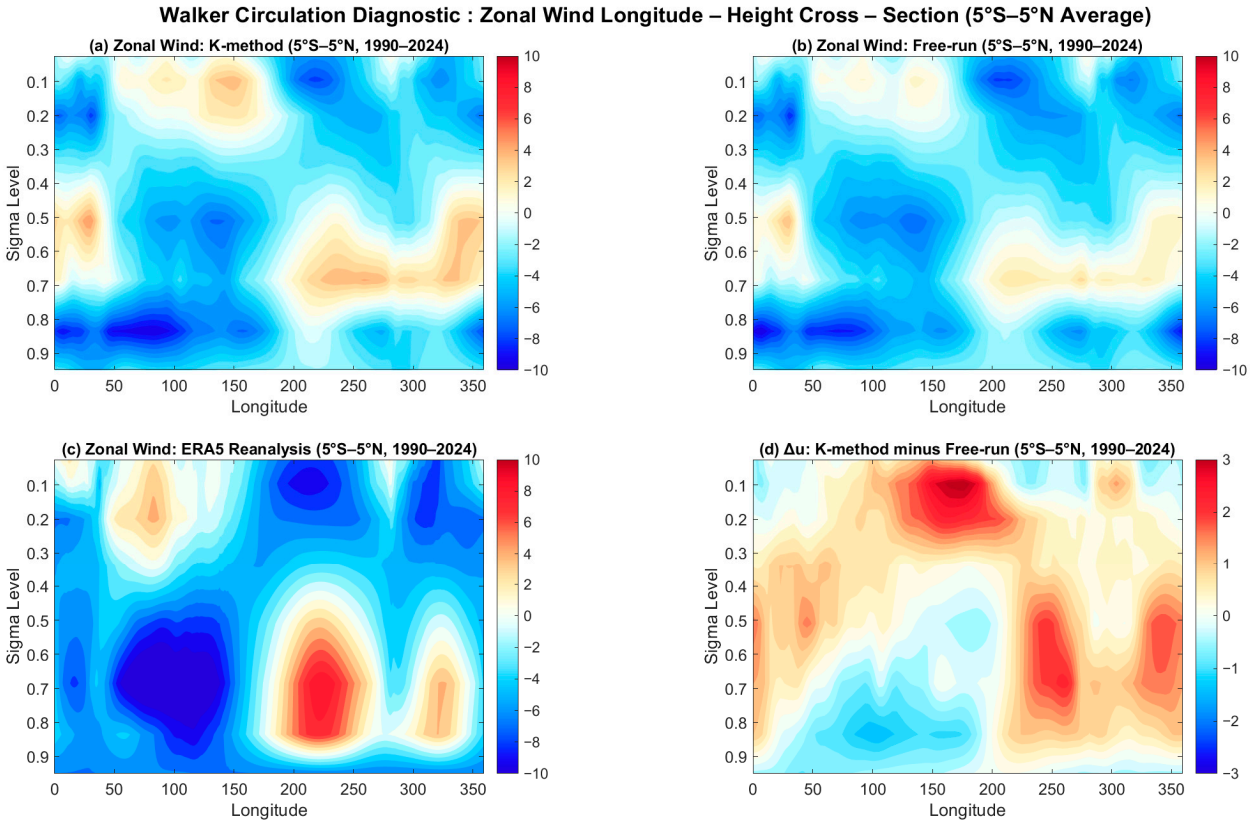

Figure 16. Walker Circulation diagnostics from longitude-height cross-sections of zonal wind averaged between 5° S and 5° N. (**a**) Zonal wind from the K-method simulation. (**b**) Zonal wind from the free-running simulation. (**c**) Zonal wind from ERA5 reanalysis for comparison. (**d**) Difference in zonal wind between the K-method and free-running simulations (Δu = K-method minus free-run). The vertical coordinate is in sigma levels (normalized pressure), with the surface at the bottom.

These diagnostics reveal a coherent physical mechanism: adaptive ocean nudging successfully improves the oceanic thermal state and provides modified moisture forcing to

the atmosphere through physically consistent adjustments in latent heat flux. However, constrained by its relatively coarse resolution and simplified parameterization schemes, the atmospheric component translates this thermal and moisture forcing into an imperfect dynamical response [21,29]. The altered structure of the Walker Circulation modifies the spatial distribution of low-level moisture convergence and vertical motion.

Therefore, the degradation of precipitation simulation is not a direct product of the boosting scheme itself, but exposes the shortcomings of parameterization within the atmospheric module of this coupled model, as well as the fundamental limitations of the current "ocean only" assimilation strategy within the coupled system. The results indicate that when there is inherent bias in the dynamic response of atmospheric models to SST forcing, improving sea conditions alone is not sufficient to achieve complete self consistent coupling simulation. This understanding strongly suggests that in the future, there is a need to develop a coupled data assimilation framework that can jointly constrain key ocean and atmospheric state variables, in order to achieve more balanced and physically consistent sea air interactions.

5. Conclusions and Discussion

Building on the traditional latitude-dependent nudging scheme, this study proposed and evaluated an adaptive nudging approach (the K method) based on a spatially heterogeneous gain matrix, implemented in the SPEEDY-NEMO coupled model. The core of this method lies in introducing a three-dimensional gain matrix, dynamically calculated from model and observational errors, and combining it with the baseline assimilation coefficient to yield a spatially varying assimilation strength. By explicitly linking nudging intensity to local error characteristics, the method ensures physically consistent corrections across different ocean regions.

Experimental results demonstrate that compared with the traditional Latmean scheme, the adaptive K method achieves more robust and systematic improvements in ocean temperature assimilation. In the upper 0–200 m subsurface, including the tropics, the North Pacific, and the North Atlantic, RMSE reductions reach 20–30%, and correlation increases up to 50%. RMSE decomposition further reveals that the K method simultaneously corrects systematic climatological biases (bias term) and enhances the representation of variability (variance term), thereby improving both mean states and temporal dynamics.

The optimization of ocean temperature also exerts positive cascading effects on other oceanic variables through dynamical and thermodynamical coupling. Improvements are evident in subsurface salinity, zonal currents, and sea surface height anomalies, confirming the pivotal role of temperature as a core state variable in constraining ocean circulation. Nevertheless, degradations in surface salinity and currents highlight the strong dependence of surface-layer variables on atmospheric forcing, which remains inadequately constrained due to the coarse resolution and lack of assimilation in the SPEEDY atmospheric module.

The study also identifies important limitations. While ocean temperature fields are substantially improved, atmospheric variables—particularly precipitation—show limited or even degraded performance. This underscores a structural limitation of ocean-only nudging: without concurrent assimilation of atmospheric states, SST signals cannot be consistently transmitted to the atmosphere.

In summary, the spatially adaptive nudging method offers a practical and effective enhancement over conventional latitude-based schemes, providing improved representations of subsurface thermal structures and related oceanic variables in intermediate-complexity models. Building on these insights, future work should advance along four key directions. First, because the present conclusions are derived from a controlled model–reanalysis comparison framework, it will be crucial to conduct follow-up validation using fully inde-

pendent observational platforms such as TAO/TRITON moorings, non-assimilated Argo profiles, and satellite-derived SST products. Such evaluations are essential for assessing the robustness of the proposed scheme under realistic observing conditions, its capability to capture regional oceanic processes, and its performance in representing extreme events. Second, the temporal adaptability of the scheme should be explored by developing a dynamic, time-varying gain matrix. Moving beyond the static climatological error estimates used here, future implementations could calculate errors over running windows or for specific seasons. This would allow the nudging strength to respond to evolving model biases during different climatic regimes, such as ENSO events or marine heatwaves, thereby addressing a key temporal limitation identified in the current study. Third, developing a vertically adaptive scheme with physical consistency is essential. Future work must move beyond the current static gain matrix to design vertically adaptive coefficients that co-evolve with local oceanic dynamical structures. This is key to fundamentally improving assimilation performance within and below the thermocline. Fourth, future efforts should explore the development of fully coupled assimilation strategies that jointly incorporate ocean temperature and key atmospheric variables. By explicitly addressing the coupled nature of SST–precipitation feedbacks, these approaches have the potential to reduce regional rainfall biases and substantially enhance the capability of intermediate-complexity models to reproduce tropical precipitation climatology.

Author Contributions: Conceptualization, Y.W. and F.Z.; methodology, Y.W. and F.Z.; software, Y.W.; model experiments, Y.W. and M.A.A.; validation, Y.W.; formal analysis, Y.W. and F.Z.; writing—original draft preparation, Y.W.; writing—review and editing, Y.W., F.Z., C.Y. and M.A.A. All authors have read and agreed to the published version of the manuscript.

Funding: This work was supported by the Jing–Jin–Ji Regional Integrated Environmental Improvement-National Science and Technology Major Project (Grant No. 2025ZD1201700) and the National Natural Science Foundation of China (Grant No. 42430114).

Data Availability Statement: The reanalysis datasets used in this study are publicly available: ORAS5 (https://cds.climate.copernicus.eu/datasets/reanalysis-oras5, accessed on 4 May 2025) and GODAS (https://psl.noaa.gov/data/gridded/data.godas.html, accessed on 4 May 2025). The model code (SPEEDY–NEMO) and experimental outputs generated during this study are available from the corresponding author upon reasonable request.

Conflicts of Interest: The authors declare no conflicts of interest.

References

1. Bindoff, N.L.; Mcdougall, T.J. Diagnosing Climate Change and Ocean Ventilation Using Hydrographic Data. *J. Phys. Oceanogr.* **1994**, *24*, 1137–1152. [CrossRef]
2. Meehl, G.A.; Arblaster, J.M.; Fasullo, J.T.; Hu, A.; Trenberth, K.E. Model-based evidence of deep-ocean heat uptake during surface-temperature hiatus periods. *Nat. Clim. Change* **2011**, *1*, 360–364. [CrossRef]
3. Buckley, M.W.; Marshall, J. Observations, inferences, and mechanisms of the Atlantic Meridional Overturning Circulation: A review. *Rev. Geophys.* **2016**, *54*, 5–63. [CrossRef]
4. Cheng, L.; Foster, G.; Hausfather, Z.; Trenberth, K.E.; Abraham, J. Improved Quantification of the Rate of Ocean Warming. *J. Clim.* **2022**, *35*, 4827–4840. [CrossRef]
5. McPhaden, M.J.; Zebiak, S.E.; Glantz, M.H. ENSO as an Integrating Concept in Earth Science. *Science* **2006**, *314*, 1740–1745. [CrossRef] [PubMed]
6. Rahmstorf, S. Ocean circulation and climate during the past 120,000 years. *Nature* **2002**, *419*, 207–214. [CrossRef]
7. Anderson, D.L.T.; Sheinbaum, J.; Haines, K. Data assimilation in ocean models. *Rep. Prog. Phys.* **1996**, *59*, 1209–1266. [CrossRef]
8. Storto, A.; Frolov, S.; Slivinski, L.; Yang, C. Correction of sea surface biases in the NEMO ocean general circulation model using neural networks. *Geosci. Model Dev.* **2025**, *18*, 4789–4804. [CrossRef]
9. Chen, X.; Wang, H.; Zheng, F.; Cai, Q. An ensemble-based SST nudging method proposed for correcting the subsurface temperature field in climate model. *Acta Oceanol. Sin.* **2020**, *39*, 73–80. [CrossRef]

10. Davies, H.C.; Turner, R.E. Updating prediction models by dynamical relaxation: An examination of the technique. *Quart. J. R. Meteorol. Soc.* **1977**, *103*, 225–245. [CrossRef]
11. Lo, J.C.; Yang, Z.; Pielke, R.A. Assessment of three dynamical climate downscaling methods using the Weather Research and Forecasting (WRF) model. *J. Geophys. Res.* **2008**, *113*, 2007JD009216. [CrossRef]
12. Ruggiero, G.A.; Ourmières, Y.; Cosme, E.; Blum, J.; Auroux, D.; Verron, J. Data assimilation experiments using the diffusive back and forth nudging for the NEMO ocean model. *Nonlinear Process. Geophys.* **2015**, *22*, 233–248. [CrossRef]
13. Zheng, F.; Zhu, J. Coupled assimilation for an intermediated coupled ENSO prediction model. *Ocean Dyn.* **2010**, *60*, 1061–1073. [CrossRef]
14. Liu, L.; Chen, X. A Spatially Dependent Nudging Method and Its Application to a Global Tide Assimilation. *Adv. Atmos. Sci.* **2024**, *41*, 2464–2477. [CrossRef]
15. Mahadevan, A. Spatial Heterogeneity and Its Relation to Processes in the Upper Ocean. In *Ecosystem Function in Heterogeneous Landscapes*; Lovett, G.M., Turner, M.G., Jones, C.G., Weathers, K.C., Eds.; Springer: New York, NY, USA, 2005; pp. 165–182. [CrossRef]
16. Dubinkina, S.; Goosse, H. An assessment of particle filtering methods and nudging for climate state reconstructions. *Clim. Past* **2013**, *9*, 1141–1152. [CrossRef]
17. Chen, Y.; Zhang, W.; Wang, P. An application of the localized weighted ensemble Kalman filter for ocean data assimilation. *Quart. J. R. Meteorol. Soc.* **2020**, *146*, 3029–3047. [CrossRef]
18. Stepanov, V.N.; Resnyanskii, Y.D.; Strukov, B.S.; Zelenko, A.A. Assimilation of Argo Profile Measurements and Sea Surface Temperature Data by the NEMO Ocean Circulation Model Using an Ensemble Kalman Filter and Three-Dimensional Variational Analysis. *Oceanology* **2025**, *65*, 364–375. [CrossRef]
19. Valcke, S. The OASIS3 coupler: A European climate modelling community software. *Geosci. Model. Dev.* **2013**, *6*, 373–388. [CrossRef]
20. Kucharski, F.; Molteni, F.; Bracco, A. Decadal interactions between the western tropical Pacific and the North Atlantic Oscillation. *Clim. Dyn.* **2006**, *26*, 79–91. [CrossRef]
21. Kucharski, F.; Molteni, F.; King, M.P.; Farneti, R.; Kang, I.-S.; Feudale, L. On the Need of Intermediate Complexity General Circulation Models: A "SPEEDY" Example. *Bull. Am. Meteorol. Soc.* **2013**, *94*, 25–30. [CrossRef]
22. Molteni, F. Atmospheric simulations using a GCM with simplified physical parametrizations. I: Model climatology and variability in multi-decadal experiments. *Clim. Dyn.* **2003**, *20*, 175–191. [CrossRef]
23. Madec, G.; NEMO System Team. *NEMO Ocean Engine*; Note du Pôle de Modélisation de L'institut Pierre-Simon Laplace (IPSL): France, 2015; pp. 61–67. Available online: https://zenodo.org/records/1464817 (accessed on 15 December 2025).
24. Anthes, R.A. The dynamics and energetics of mature tropical cyclones. *Rev. Geophys.* **1974**, *12*, 495–522. [CrossRef]
25. Holland, W.R.; Malanotte-Rizzoli, P. Assimilation of Altimeter Data into an Ocean Circulation Model: Space versus Time Resolution Studies. *J. Phys. Oceanogr.* **1989**, *19*, 1507–1534. [CrossRef]
26. Verron, J. Altimeter data assimilation into an ocean circulation model: Sensitivity to orbital parameters. *J. Geophys. Res.* **1990**, *95*, 11443–11459. [CrossRef]
27. Keenlyside, N.; Latif, M.; Botzet, M.; Jungclaus, J.; Schulzweida, U. A coupled method for initializing El Niño Southern Oscillation forecasts using sea surface temperature. *Tellus A Dyn. Meteorol. Oceanogr.* **2005**, *57*, 340. [CrossRef]
28. Taylor, K.E. Summarizing multiple aspects of model performance in a single diagram. *J. Geophys. Res.* **2001**, *106*, 7183–7192. [CrossRef]
29. Ruggieri, P.; Abid, M.A.; García-Serrano, J.; Grancini, C.; Kucharski, F.; Pascale, S.; Volpi, D. SPEEDY-NEMO: Performance and applications of a fully-coupled intermediate-complexity climate model. *Clim. Dyn.* **2024**, *62*, 3763–3781. [CrossRef]
30. Zuo, H.; Balmaseda, M.A.; Tietsche, S.; Mogensen, K.; Mayer, M. The ECMWF operational ensemble reanalysis–analysis system for ocean and sea ice: A description of the system and assessment. *Ocean Sci.* **2019**, *15*, 779–808. [CrossRef]
31. Hersbach, H.; Bell, B.; Berrisford, P.; Hirahara, S.; Horányi, A.; Muñoz-Sabater, J.; Nicolas, J.; Peubey, C.; Radu, R.; Schepers, D.; et al. The ERA5 global reanalysis. *Quart. J. R. Meteorol. Soc.* **2020**, *146*, 1999–2049. [CrossRef]
32. Song, X.; Li, X.; Zhang, S.; Li, Y.; Chen, X.; Tang, Y.; Chen, D. A new nudging scheme for the current operational climate prediction system of the National Marine Environmental Forecasting Center of China. *Acta Oceanol. Sin.* **2022**, *41*, 51–64. [CrossRef]
33. Chen, N.; Fang, X. A Simple Multiscale Intermediate Coupled Stochastic Model for El Niño Diversity and Complexity. *J. Adv. Model. Earth Syst.* **2023**, *15*, e2022MS003469. [CrossRef]
34. Zhang, Y.; Chen, N.; Moser, C. A Simple Intermediate Coupled MJO-ENSO Model: Multiscale Interactions and ENSO Complexity 2025. *arXiv* **2025**, arXiv:2507.14395. [CrossRef]
35. Gao, H.; Duan, J. Dynamics of a coupled atmosphere–ocean model. *Nonlinear Anal. Real. World Appl.* **2004**, *5*, 667–693. [CrossRef]
36. Ricchi, A.; Miglietta, M.M.; Bonaldo, D.; Cioni, G.; Rizza, U.; Carniel, S. Multi-Physics Ensemble versus Atmosphere–Ocean Coupled Model Simulations for a Tropical-Like Cyclone in the Mediterranean Sea. *Atmosphere* **2019**, *10*, 202. [CrossRef]

37. van Aken, H.M. The Oceanic Thermohaline Circulation: An Introduction. In *Atmospheric and Oceanographic Sciences Library*; Springer: New York, NY, USA, 2007.
38. Kawai, Y.; Hosoda, S.; Uehara, K.; Suga, T. Heat and salinity transport between the permanent pycnocline and the mixed layer due to the obduction process evaluated from a gridded Argo dataset. *J. Oceanogr.* **2021**, *77*, 75–92. [CrossRef]
39. Oh, J.-H.; Kug, J.-S.; An, S.-I.; Jin, F.-F.; McPhaden, M.J.; Shin, J. Emergent climate change patterns originating from deep ocean warming in climate mitigation scenarios. *Nat. Clim. Change* **2024**, *14*, 260–266. [CrossRef]
40. Yu, L.; Josey, S.A.; Bingham, F.M.; Lee, T. Intensification of the global water cycle and evidence from ocean salinity: A synthesis review. *Ann. N. Y. Acad. Sci.* **2020**, *1472*, 76–94. [CrossRef]
41. Gera, A.; Mitra, A.K.; Mahapatra, D.K.; Momin, I.M.; Rajagopal, E.N.; Basu, S. Sea surface height anomaly and upper ocean temperature over the Indian Ocean during contrasting monsoons. *Dyn. Atmos. Ocean.* **2016**, *75*, 1–21. [CrossRef]
42. Widlansky, M.J.; Long, X.; Schloesser, F. Increase in sea level variability with ocean warming associated with the nonlinear thermal expansion of seawater. *Commun. Earth Environ.* **2020**, *1*, 9. [CrossRef]
43. Sardana, D.; Kumar, P. Rajni CMIP6 model evaluation for sea surface height responses to ENSO. *Clim. Dyn.* **2024**, *62*, 1829–1847. [CrossRef]
44. Kumar, P.; Sardana, D.; Weller, E.; Bhaskaran, P.K. Influence of climate variability on sea level rise and its teleconnection with sea surface temperature anomalies over the Indo-Pacific Ocean. *Int. J. Climatol.* **2022**, *42*, 10195–10216. [CrossRef]
45. Woods Hole Oceanographic Institution; Farrar, J.T.; Plueddmann, A. On the Factors Driving Upper-Ocean Salinity Variability at the Western Edge of the Eastern Pacific Fresh Pool. *Oceanography* **2019**, *32*, 30–39. [CrossRef] [PubMed]
46. Yao, S.-L.; Wu, R.; Luo, J.-J.; Zhou, W. Competing impacts of tropical Pacific and Atlantic on Southern Ocean inter-decadal variability. *npj Clim. Atmos. Sci.* **2024**, *7*, 104. [CrossRef]
47. Roemmich, D.; Gilson, J. The 2004–2008 mean and annual cycle of temperature, salinity, and steric height in the global ocean from the Argo Program. *Prog. Oceanogr.* **2009**, *82*, 81–100. [CrossRef]
48. Hamlington, B.D.; Cheon, S.H.; Piecuch, C.G.; Karnauskas, K.B.; Thompson, P.R.; Kim, K.-Y.; Reager, J.T.; Landerer, F.W.; Frederikse, T. The Dominant Global Modes of Recent Internal Sea Level Variability. *JGR Ocean.* **2019**, *124*, 2750–2768. [CrossRef]
49. Thual, S.; Dewitte, B.; Ayoub, N.; Thual, O. An Asymptotic Expansion for the Recharge–Discharge Model of ENSO. *J. Phys. Oceanogr.* **2013**, *43*, 1407–1416. [CrossRef]
50. Dewitte, B.; Yeh, S.-W.; Thual, S. Reinterpreting the thermocline feedback in the western-central equatorial Pacific and its relationship with the ENSO modulation. *Clim. Dyn.* **2013**, *41*, 819–830. [CrossRef]
51. Kelemen, F.D.; Primo, C.; Feldmann, H.; Ahrens, B. Added Value of Atmosphere-Ocean Coupling in a Century-Long Regional Climate Simulation. *Atmosphere* **2019**, *10*, 537. [CrossRef]
52. Tong, J.; Zheng, F.; Jin, J.; Yang, R.; Zhu, J.; Zeng, Q. The source of Double ITCZ induced by the SST bias over the tropical western Pacific as reflected in CAS-ESM2 Model. *Sci. China Earth Sci.* **2024**, *67*, 1604–1615. [CrossRef]
53. Chen, D.; Lian, T.; Fu, C.; Cane, M.A.; Tang, Y.; Murtugudde, R.; Song, X.; Wu, Q.; Zhou, L. Strong influence of westerly wind bursts on El Niño diversity. *Nat. Geosci.* **2015**, *8*, 339–345. [CrossRef]
54. Fernández, P.; Speich, S.; Bellenger, H.; Lange Vega, D.; Karstensen, J.; Zhang, D.; Rocha, C.B. On the Mechanisms Driving Latent Heat Flux Variations in the Northwest Tropical Atlantic. *JGR Ocean.* **2024**, *129*, e2023JC020658. [CrossRef]
55. Vivant, F.; Siegelman, L.; Klein, P.; Torres, H.S.; Menemenlis, D.; Molod, A.M. Ocean submesoscale fronts induce diabatic heating and convective precipitation within storms. *Commun. Earth Environ.* **2025**, *6*, 69. [CrossRef]